

<sub>1</sub> Study of neutrino-nucleus interaction at around 1 GeV using  
<sub>2</sub> a 3D grid-structure neutrino detector, WAGASCI, muon  
<sub>3</sub> range detectors and magnetized spectrometer, Baby MIND,  
<sub>4</sub> at J-PARC neutrino monitor hall

<sub>5</sub> A. Bonnemaison, R. Cornat, L. Domine, O. Drapier, O. Ferreira, F. Gastaldi,  
<sub>6</sub> M. Gonin, J. Imber, M. Licciardi, F. Magniette, T. Mueller, L. Vignoli, and O. Volcy  
<sub>7</sub> *Ecole Polytechnique, IN2P3-CNRS, Laboratoire Leprince-Ringuet, Palaiseau,*  
<sub>8</sub> *France*

<sub>9</sub> S. Cao and T. Kobayashi

<sub>10</sub> *High Energy Accelerator Research Organization (KEK), Tsukuba, Ibaraki, Japan*

<sub>11</sub> M. Khabibullin, A. Khotjantsev, A. Kostin, Y. Kudenko, A. Mefodiev, O. Mineev,  
<sub>12</sub> S. Suvorov, and N. Yershov

<sub>13</sub> *Institute for Nuclear Research of the Russian Academy of Sciences, Moscow, Russia*

<sub>14</sub> B. Quilain

<sub>15</sub> *Kavli Institute for the Physics and Mathematics of the Universe (WPI), The*  
<sub>16</sub> *University of Tokyo Institutes for Advanced Study, University of Tokyo, Kashiwa,*  
<sub>17</sub> *Chiba, Japan*

<sub>18</sub> T. Hayashino, A. Hiramoto, A.K. Ichikawa, K. Nakamura, T. Nakaya, K Yasutome,  
<sub>19</sub> and K. Yoshida

<sub>20</sub> *Kyoto University, Department of Physics, Kyoto, Japan*

<sub>21</sub> Y. Azuma, J. Harada, T. Inoue, K. Kin, N. Kukita, S. Tanaka, Y. Seiya,  
<sub>22</sub> K. Wakamatsu, and K. Yamamoto

<sub>23</sub> *Osaka City University, Department of Physics, Osaka, Japan*

24 A. Blondel, F. Cadoux, Y. Favere, E. Noah, L. Nicola, and S. Parsa

25 *University of Geneva, Section de Physique, DPNC, Geneva, Switzerland*

26 N. Chikuma, F. Hosomi, T. Koga, R. Tamura, and M. Yokoyama

27 *University of Tokyo, Department of Physics, Tokyo, Japan*

28 Y. Hayato

29 *University of Tokyo, Institute for Cosmic Ray Research, Kamioka Observatory,  
30 Kamioka, Japan*

31 Y. Asada, K. Matsushita, A. Minamino, K. Okamoto, and D. Yamaguchi

32 *Yokohama National University, Faculty of Engineering, Yokohama, Japan*

33 December 14, 2017

34 **Contents**

35	<b>1</b>	<b>Introduction</b>	<b>3</b>
36	<b>2</b>	<b>Experimental Setup</b>	<b>4</b>
37	2.1	Wagasci module . . . . .	5
38	2.2	INGRID Proton module . . . . .	6
39	2.3	Baby MIND . . . . .	9
40	2.3.1	Magnet modules . . . . .	9
41	2.3.2	Scintillator modules . . . . .	10
42	2.3.3	Electronics . . . . .	12
43	2.3.4	Pefromance check . . . . .	13
44	2.4	Side muon range detector . . . . .	14
45	<b>3</b>	<b>Physics goals</b>	<b>16</b>
46	3.1	Expected number of events . . . . .	17
47	3.2	Pseudo-monochromatic beam by using different off-axis fluxes . . . . .	17
48	3.3	Subjects Wagasci can contribute . . . . .	18

49	<b>4 Status of J-PARC T59 experiment</b>	<b>19</b>
50	<b>5 MC studies</b>	<b>21</b>
51	5.1 Detector simulation . . . . .	21
52	5.1.1 Detector geometry . . . . .	22
53	5.1.2 Response of detector components . . . . .	22
54	5.2 Track reconstruction . . . . .	23
55	5.3 Event selection . . . . .	23
56	5.4 Cross section measurements on water . . . . .	26
57	5.4.1 Charged current cross section measurement . . . . .	27
58	<b>6 Standalone WAGASCI-module performances</b>	<b>27</b>
59	6.1 Reconstruction algorithm . . . . .	30
60	6.1.1 Description . . . . .	30
61	6.1.2 Performances . . . . .	32
62	6.2 Background subtraction: the water-out module . . . . .	39
63	<b>7 Schedule</b>	<b>42</b>
64	<b>8 Requests</b>	<b>42</b>
65	8.1 Neutrino beam . . . . .	42
66	8.2 Equipment request including power line . . . . .	42
67	8.2.1 Baby MIND Equipment request including power line . . . . .	43
68	<b>9 Conclusion</b>	<b>43</b>

## 69 **1 Introduction**

70 The understanding of neutrino-nucleus interactions in the 1 GeV energy region is critical  
 71 for the success of accelerator-based neutrino oscillation experiments such as the T2K exper-  
 72 iment. Complicated multi-body effects of nuclei render this understanding difficult. The  
 73 T2K near detectors have been measuring these and significant progress has been achieved.  
 74 However, the understanding is still limited. One of the big factors preventing from full  
 75 understanding is the non-monochromatic neutrino beam spectrum. Measurements with  
 76 different but some overlapping beam spectra would greatly benefit to resolve the contri-  
 77 bution from different neutrino energies. We, the Wagasci collaboration, proposes to study  
 78 the neutrino-nucleus interaction at the B2 floor of the neutrino monitor building, where  
 79 different neutrino spectra can be obtained due to the different off-axis position. Our exper-  
 80 imental setup contains 3D grid-structure plastic-scintillator detectors filled with water as  
 81 the neutrino interaction target (Wagasci modules), two side- and one downstream- muon  
 82 range detectors(MRD's). The 3D grid-structure and side-MRD's allows a measurement of

wider-angle scattering than the T2K off-axis near detector (ND280). High water to scintillator material ratio enables the measurement of the neutrino interaction on water, which is highly desired for the T2K experiment because it's far detector, Super-Kamiokande, is composed of water. The MRD's consist of plastic scintillators and iron plates. The downstream-MRD, so called the Baby MIND detector, also works as a magnet and provides the charge identification capability as well as magnetic momentum measurement for high energy muons. The charge identification is essentially important to select antineutrino events in the antineutrino beam because contamination of the neutrino events is as high as 30%. Most of the detectors has been already constructed. The Wagasci modules have been commissioned as the J-PARC T59 experiment and the Baby MIND detector was commissioned at the CERN neutrino platform. Therefore, the collaboration will be ready to proceed to the physics data taking for the T2K beam time in January 2019. We will provide the cross sections of the charged current neutrino and antineutrino interactions on water with slightly higher neutrino energy than T2K ND280 with wide angler acceptance. When combined with ND280 measurements, our measurement would greatly improve the understanding of the neutrino interaction at around 1 GeV and contribute to reduce one of the most significant uncertainty of the T2K experiment.

## 2 Experimental Setup

Figure. 1 and 2 show a schematic view and a CAD drawing of the entire set of detectors. Central neutrino target detectors consist of two Wagasci modules and T2K INGRID proton module. Inside the Wagasci module, plastic scintillator bars are aligned as a 3D grid-like structure and spaces in the structure are filled with water for a water-in Wagasci module. T2K INGRID proton module is a full active neutrino target detector which is composed only with scintillator bars in its tracking region. The central detectors are surrounded by two side- and one downstream- muon range detectors(MRD's) The MRD's are used to select muon tracks from the charged-current (CC) interactions and to reject short tracks caused by neutral particles that originate mainly from neutrino interactions in material surrounding the central detector, like the walls of the detector hall, neutrons and gammas, or neutral-current (NC) interactions. The muon momentum can be reconstructed from its range inside the detector. The MRD's consist of plastic scintillators and iron plates. In addition, each of the iron plates of the downstream-MRD, so called the Baby MIND detector, is wound by a coil and can be magnetized. It provide the charge selection capability.

For all detectors, scintillation light in the scintillator bar is collected and transported to a photodetector with a wavelength shifting fiber (WLS fiber). The light is read out by a photodetector, Multi-Pixel Photon Counter (MPPC), attached to one end of the WLS fiber. The signal from the MPPC is read out by the dedicated electronics developed for the test experiment to enable bunch separation in the beam spill. The readout electronics is triggered using the beam-timing signal from MR to synchronize to the beam. The beam-

121 timing signal is branched from those for T2K, and will not cause any effect on the T2K  
122 data taking.

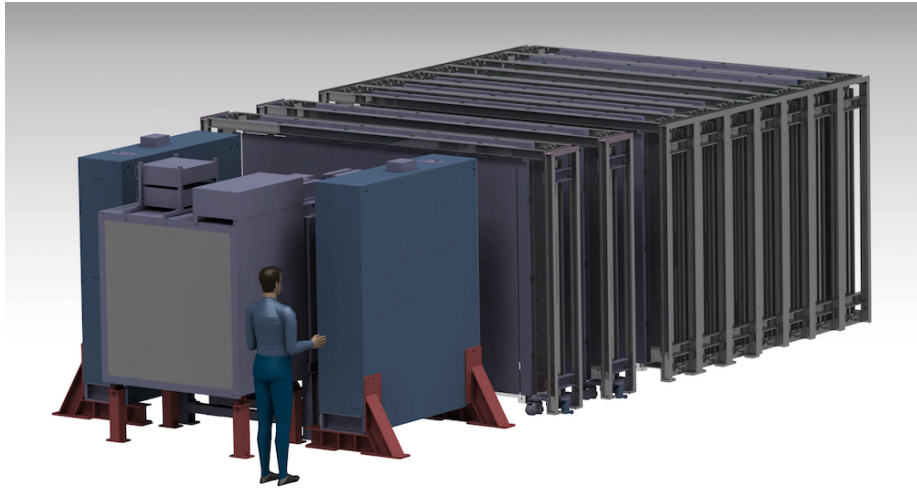


Figure 1: Schematic view of entire sets of detectors.

123 T2K adopted the off-axis beam method, in which the neutrino beam is intentionally  
124 directed 2.5 degrees away from SK producing a narrow band  $\nu_\mu$  beam. The off-axis near  
125 detector, ND280, is installed towards the SK direction in the B1 floor of the near detector  
126 hall of the J-PARC neutrino beam-line. We propose to install our detector in the B2 floor  
127 of the near detector hall, where the off-axis angle is similar but slightly different: 1.5 degree.  
128 The candidate detector position in the B2 floor is shown in Fig. 3. The expected neutrino  
129 energy spectrum at the candidate position is shown in Fig. 4.

## 130 2.1 Wagasci modules

131 The Wagasci modules are neutrino target detector consists of 16 scintillator tracking planes,  
132 where each plane is an array of 80 scintillator bars. The total number of channels in one  
133 Wagasci module is 1280. The 40 bars, called parallel scintillators, are placed perpendic-  
134 ularly to the beam, and the other 40 bars, called grid scintillators, are placed in parallel  
135 to the beam with grid structure in the tracking plane as shown in Fig. 5. Thanks to  
136 the 3 D grid-like structure of the scintillator bars, the Wagasci module has  $4\pi$  angular  
137 acceptance for charged particles. Thin plastic scintillator bars (3 mm in thickness, Figure  
138 6) are used for the Wagasci modules to reduce the mass ratio of scintillator bars to water,  
139 because neutrino interactions in the scintillator bars are a background for the cross section  
140 measurements on H<sub>2</sub>O. The dimension of the each Wagasci module is 125cm × 125cm in  
141 the x and y directions and 46cm along the beam direction as shown in 5.

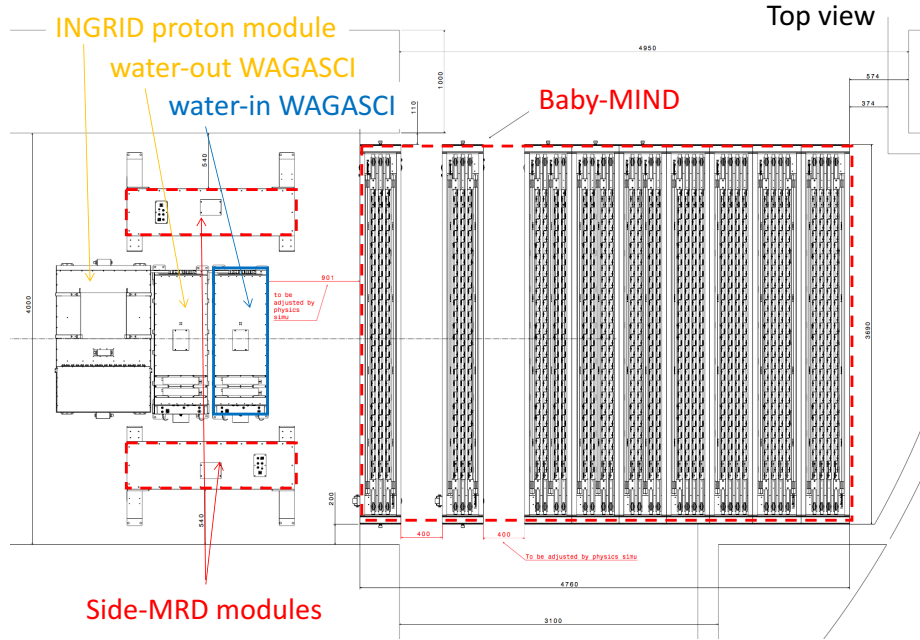


Figure 2: Top view of entire sets of detectors.

We will have two types of the Wagasci modules, a water-in module and a water-out module. The water-in Wagasci module has water in spaces of the grid structure. The total water mass serving as neutrino targets in the fiducial volume of the module is 188 kg, and the mass ratio of scintillator bars to water is 80 %. The water-out Wagasci module doesn't have water inside the detector. The total CH mass serving as neutrino target in the fiducial volume of the module is 47 kg, and the mass fraction of scintillator bars is 100 %.

148 2.2 INGRID Proton module

149 INGRID Proton module is a neutrino detectors of the T2K experiment. It is a fully-active  
 150 tracking detector which consists of only scintillator strips. The purpose of this Proton  
 151 Module is to separate the neutrino interaction types by detecting the protons and pions  
 152 together with the muons from the neutrino interactions, and to measure the neutrino cross  
 153 section for each interaction type. It consists of 36 tracking planes surrounded by veto planes  
 154 (Figure 7), where each tracking plane is an array of two types of scintillator strips. The  
 155 16 strips in the inner region have dimensions of  $2.5\text{cm} \times 1.3\text{cm} \times 120\text{cm}$ , while the 16 strips  
 156 in the outer region have dimensions of  $5\text{cm} \times 1\text{cm} \times 120\text{cm}$ , making a plane of  $120 \times 120\text{cm}^2$   
 157 in the horizontal and vertical directions. The former is the scintillator produced for the

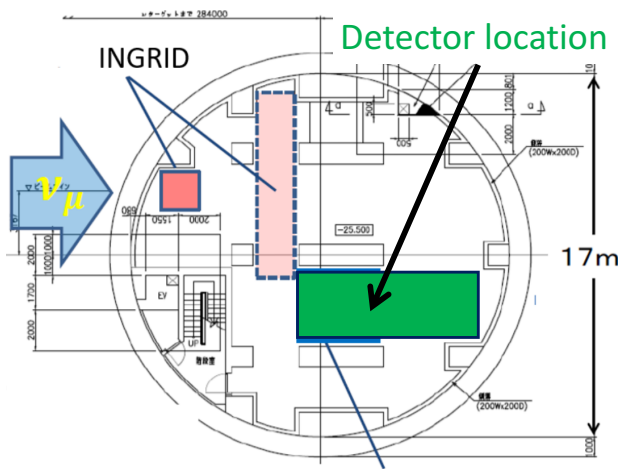


Figure 3: Candidate detector position in the B2 floor of the near detector hall.

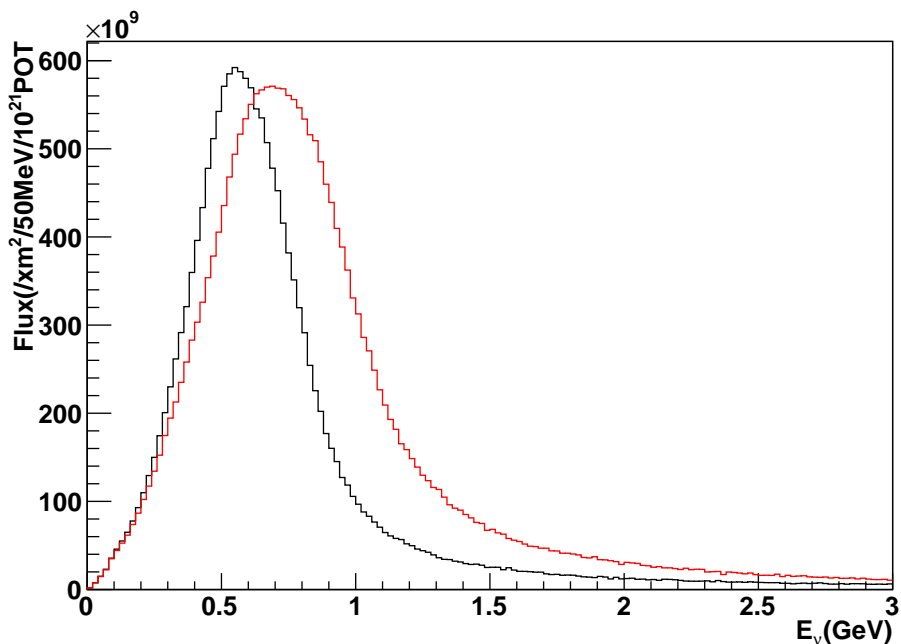


Figure 4: Neutrino energy spectrum at the candidate detector position (red, off-axis 1.5 degree). The spectrum at the ND280 site (black, off-axis 2.5 degree) is also shown.

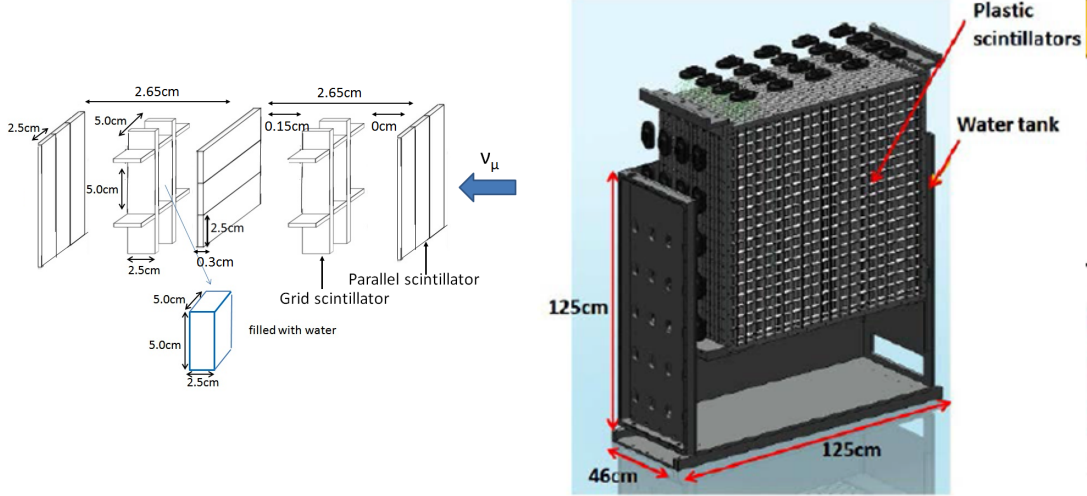


Figure 5: Schematic views of 3D grid-like structure of plastic scintillator bars (left) and Wagasci module (right).

158 K2K SciBar detector [3] and the latter was produced for INGRID. The tracking planes are  
 159 placed perpendicular to the beam axis at 23mm intervals. Since the strips are aligned in one  
 160 direction, each tracking plane is sensitive to either the horizontal or vertical position of the  
 161 tracks. The tracking planes are therefore placed alternating in the horizontal and vertical  
 162 directions so that three-dimensional tracks can be reconstructed. The tracking planes also  
 163 serve as the neutrino interaction target. As with the Wagasci modules, scintillation light  
 164 is read out by a WLS fiber and MPPC.

165 It was installed at the neutrino beam axis on the SS floor of the T2K near detector hall  
 166 in 2010, and had been used for neutrino cross section measurements. In August 2017, it  
 167 was moved to the B2 floor of the T2K near detector hall by J-PARC T59 after getting the  
 168 approval from T2K to use them. J-PARC T59 is performing a neutrino beam measurement  
 169 using the detector from October 2017, and the measurement will continue until May 2018  
 170 as we will discuss in Sec. 4.

### 171 2.3 Baby MIND

172 The Baby MIND is the downstream Muon Range Detector. It also works as a magnet and  
 173 provides the charge identification capability as well as magnetic momentum measurement  
 174 for high energy muons.

175 The Baby MIND collaboration <sup>1</sup> submitted a proposal to the SPSC at CERN, SPSC-P-

---

<sup>1</sup>Contact person: E. Noah, Spokesperson: A. Blondel, Deputy spokesperson: Y. Kudenko

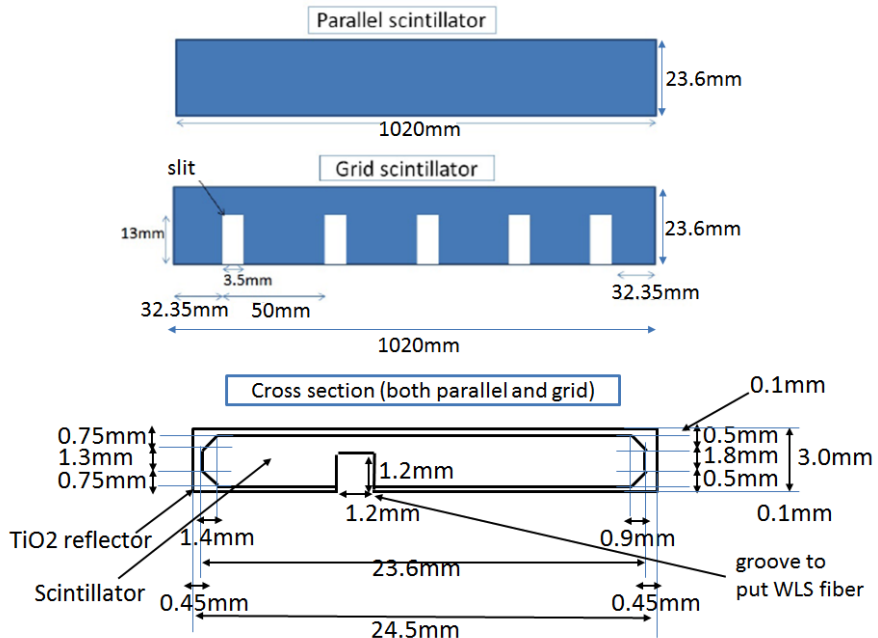


Figure 6: Geometry of scintillators used for Wagasci modules.

353. The project was approved by the CERN research board as Neutrino Platform project  
 176 NP05 and constructed. The detector consists of 33 magnet modules, each 3500 mm ×  
 177 2000 mm × 50 mm (30 mm steel) with a mass of approximately 2 tonnes. Of these magnet  
 178 modules, 18 are instrumented with plastic scintillator modules.  
 179

### 180 2.3.1 Magnet modules

181 The Baby MIND is built from sheets of iron interleaved with scintillator detector modules  
 182 but unlike traditional layouts for magnetized iron neutrino detectors (e.g. MINOS) which  
 183 tend to be monolithic blocks with a unique pitch between consecutive steel segments and  
 184 large conductor coils threaded around the whole magnet volume, the Baby MIND iron seg-  
 185 ments are all individually magnetized as shown in Fig. 8, allowing for far greater flexibility  
 186 in the setting of the pitch between segments, and in the allowable geometries that these  
 187 detectors can take.

188 The key design outcome is a highly optimized magnetic field map. A double-slit con-  
 189 figuration for coil winding was adopted to increase the area over which the magnetic flux  
 190 lines are homogeneous in  $B_x$  across the central tracking region. Simulations show the  
 191 magnet field map to be very uniform over this central tracking region covering an area of  
 192  $2800 \times 2000 \text{ mm}^2$ , Fig. 9. The  $B_x$  component dominates in this region, with negligible  $B_y$

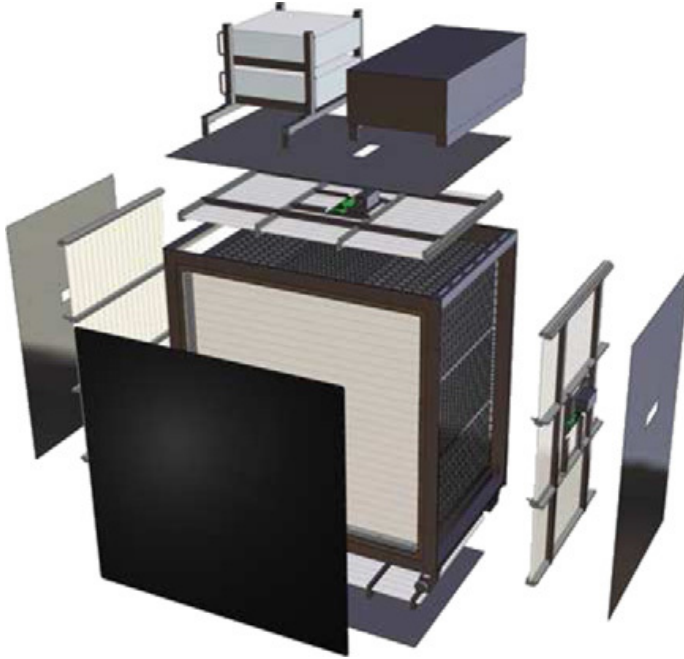


Figure 7: Schematic view of INGRID Proton module.

and  $B_z$ . This was confirmed by measuring the field with 9 pick-up coils wound around the first module. Subsequent modules were equipped with one pick-up coil. Test results on the 33 modules show all to achieve the required field of 1.5 T for a current of 140 A, with a total power consumption of 11.5 kW. The polarity of the field map shown in Fig. 9 (middle) can be reversed by changing the power supply configuration.

### 2.3.2 Scintillator modules

Each of the 18 scintillator modules is constructed from 2 planes of horizontal counters (95 counters in total) and 2 planes of vertical counters (16 counters in total) [2], arranged with an overlap between planes to achieve close to 100% hit efficiency for minimum ionizing muons. The arrangement of planes within a module is vertical-horizontal-horizontal-vertical. This arrangement was the result of an assembly approach whereby each plane was built from 2 half-planes, with each half plane consisting of a horizontal plane and a vertical plane. The scintillator bars are held in place using structural ladders that align and maintain the counters, Fig. 10. No glue is used in the process, so counters can be replaced. Aluminum sheets front and back provide light tightness.

The plastic scintillator counters were made from 220 mm-wide slabs, consisting of extruded polystyrene doped with 1.5% paraterphenyl (PTP) and 0.01% POPOP. They were

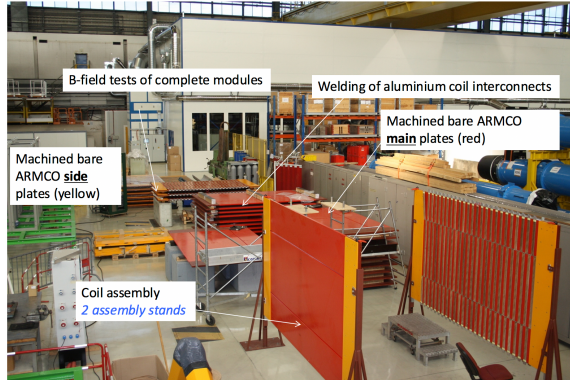


Figure 8: Magnet assembly zone at CERN.

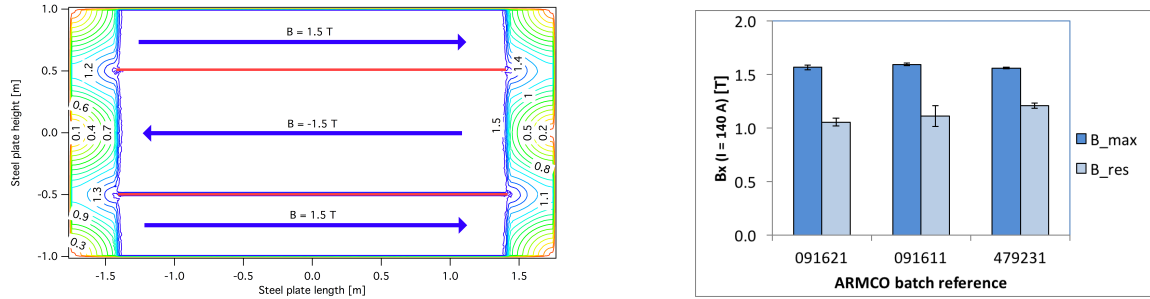


Figure 9: Left) Magnetic field map with a coil along 280 cm of the length of the plate. Right) Measured B field for 33 modules.



Figure 10: Scintillator modules assembly. Left) top of front half-module showing vertical counters, and the spacers-ladders that set the pitch between horizontal counters and hold them in place. Middle) rear half-module showing horizontal counters on their ladders. Right) Assembled rear half-module, the front half-module can be seen in the background.

210 cut to size then covered with a 30-100  $\mu\text{m}$  thick diffuse reflector resulting from etching of  
 211 the surface with a chemical agent [6, 7]. The horizontal counter size is  $2880 \times 31 \times 7.5 \text{ mm}^3$ ,  
 212 with one groove along the length of the bar in which sits a wavelength shifting fiber from  
 213 Kuraray. The vertical counter size is  $1950 \times 210 \times 7.5 \text{ mm}^3$ , with one U-shaped groove  
 214 along the bar. On each counter, two custom connectors house silicon photomultipliers,  
 215 MPPC type S12571-025C from Hamamatsu, either side of the horizontal counter, and  
 216 both connectors at the top for the vertical counter. This geometrical configuration for  
 217 vertical counters was chosen for ease of connectivity to the electronics, and maintenance  
 218 operations.

219 A total of 1744 horizontal counters and 315 vertical counters (including spares) were  
 220 produced at the Uniplast company (Vladimir, Russia).

### 221 2.3.3 Electronics

222 The Baby MIND electronic readout scheme includes several custom-designed boards [8].  
 223 The revised version is shown in Fig. 11. At the heart of the system is the electronics  
 224 Front End Board (FEB), developed by the University of Geneva. The readout system  
 225 includes two ancillary boards, the Backplane, and the Master Clock Board (MCB) whose  
 226 development has been managed by INRNE (Bulgarian Academy of Sciences) collaborators.

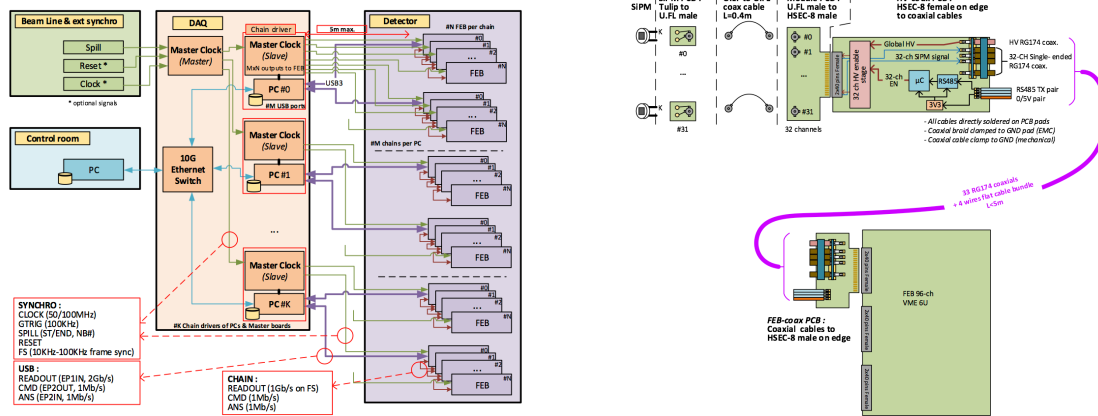


Figure 11: Left) Baby MIND electronics readout scheme. Right) SiPM-to-FEB connectivity.

227 The FEBv2 hosts 3 CITIROC chips that can each read in signals from 32 SiPMs [4].  
 228 Each signal input is processed by a high gain, and a separate low gain, signal path. The  
 229 outputs from the slow shapers can be sampled using one of two modes: a mode with an  
 230 externally applied delay, and a peak detector mode. A faster shaper can be switched to  
 231 either HG or LG paths, followed by discriminators with adjustable thresholds providing 32  
 232 individual trigger outputs and one OR32 trigger output. An Altera ARIA5 FPGA on the

233 FEBv2 samples these trigger outputs at 400 MHz, recording rising and falling times for  
234 the individual triggers and assigning time stamps to these. Time-over-threshold from the  
235 difference between falling and rising times gives some measure of signal amplitude, used in  
236 addition to charge information and useful if there is more than one hit per bar within the  
237 deadtime due to the readout of the multiplexed charge output of  $\sim 9 \mu\text{s}$ . The ARIA5 also  
238 manages the digitization of the sampled CITIROC multiplexed HG and LG outputs via a  
239 12-bit 8-ch ADC.

240 The internal 400 MHz clock on the FEBv2 can be synchronized to a common 100 MHz  
241 clock. The synchronization subsystem combines input signals from the beam line into  
242 a digital synchronization signal (SYNC) and produces a common detector clock (CLK)  
243 which can eventually be synchronised to an external experiment clock. Both SYNC and  
244 CLK signals are distributed to the FEBs. Tests show the FEB-to-FEB CLK(SYNC) delay  
245 difference to be 50 ps (70 ps). Signals from the beam line at WAGASCI include two  
246 separate timing signals, arriving 100 ms and 30  $\mu\text{s}$  before the neutrino beam at the near  
247 detectors. The spill number is available as a 16-bit signal.

#### 248 **2.3.4 Pefromance check**

249 All counters were measured at INR Moscow with a cosmic ray setup using the same type  
250 S12571-025C MPPCs and CAEN DT5742 digitizer. The average light yield (sum from both  
251 ends) was measured to be 37.5 photo-electrons (p.e.) per minimum ionizing particle (MIP)  
252 and 65 p.e./MIP for vertical and horizontal counters, respectively. After shipment to  
253 CERN, all counters were tested once more individually with an LED test setup [?]. 0.1% of  
254 counters failed the LED tests and were therefore not used during the assembly of modules.  
255 The assembly of modules was completed in June 2017, and it was then tested in June and  
256 July 2017 at the Proton Synchrotron experimental hall at CERN with a mixed particle  
257 beam comprising mostly muons whose momenta could be selected between 0.5 and 5 GeV/c.  
258 An event display from the summer 2017 tests is shown in Fig. 12.

### 259 **2.4 Side muon range detector**

260 Two Side-MRD modules for tracking secondary particles from neutrino interactions will be  
261 installed in 2018. Each Side-MRD module is composed of 11 steel plates and 10 layers of  
262 total 80 scintillator slabs installed in 13 mm gaps between the 30 mm thick plates. Each  
263 steel plate size is  $30 \times 1610 \times 1800 \text{ mm}^3$ . Total module size is  $2236 \times 1630 \times 975 \text{ mm}^3$  as  
264 shown in Fig. 13 (left), weight is  $\sim 8.5$  ton.

265 Scintillator bars were manufactured by Uniplast company in Vladimir, Russia. Polystyrene  
266 based scintillators were extruded with thickness of 7 mm, then cut to the size of  $7 \times 200 \times$   
267  $1800 \text{ mm}^3$ . Dopant composition is 1.5% PTP and 0.01% POPOP. Scintillator surface was  
268 etched by a chemical agent to form a white diffuse layer with excellent reflective perfor-  
269 mance. Ideal contact between the scintillator and the reflector raises the light yield up to

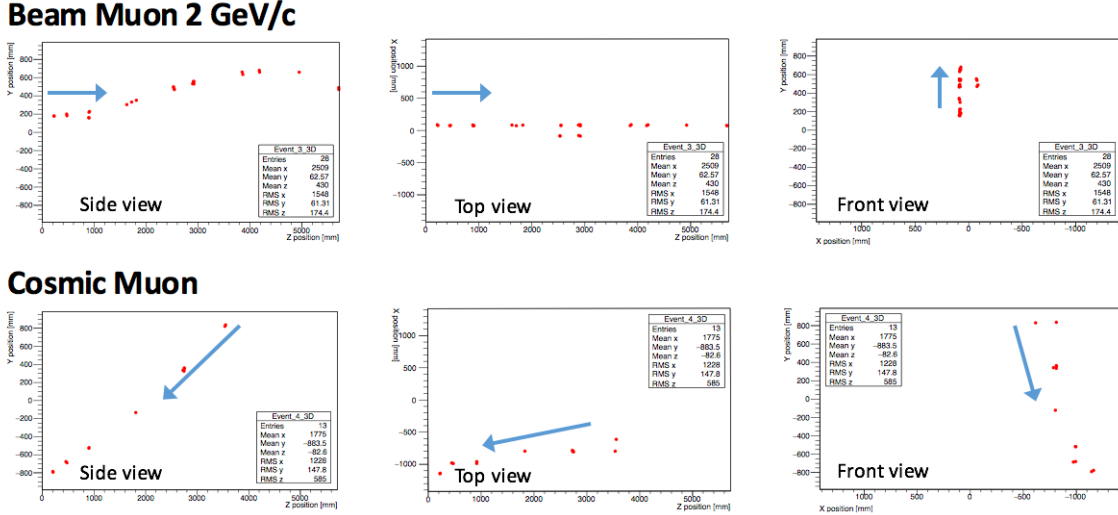


Figure 12: Comparison of a beam muon and cosmic muon in the three different geometrical projections of the detector. The beam impinges on the detector from the left. The arrows indicate the direction of travel of these muons. The direction of the cosmic muon is inferred from timing information.

50% comparing to an uncovered scintillator. Sine like groove was milled along the scintillator to provide uniform light collection over the whole scintillator surface. WLS Y11 Kuraray fiber of 1 mm diameter is glued with an optical cement EJ-500 in the S-shape groove as shown in Fig. 13(right). Bending radius is fixed to 30 mm that was specified to be safe for Kuraray S-type fibers. Both ends of the fiber are glued into optical connectors which mounted within a scintillator body and provide an interface to SiPMs, Hamamatsu MPPC S13081-050CS(X1).

Scintillators for the Side-MRD modules had been assembled at INR in Russia, and shipped to Japan in July 2017. The light yield for each scintillator was measured with cosmic rays at INR and at YNU in Japan after delivery. Parameters measured at the center of the counter were : the light yields  $LY_1$  and  $LY_2$  at both ends, the light yield asymmetry between the ends calculated as  $100\% \times \frac{LY_1 - LY_2}{LY_1 + LY_2}$ . After tests at INR we selected 324 counters from measured 332 ones with the mean light yield of 45 p.e./MIP ( $LY_1 + LY_2$ ) and the asymmetry value less than 10 %. The measurements at YNU yielded the average total light yield of about 40 p.e./MIP which varies in range from 32 to 50 p.e./MIP (Fig. 14 (left)). Only two counters showed relatively high asymmetry close to 25 % as shown in Fig. 14 (right). Using the results of the quality assurance test we selected 320 scintillator counters for the Side-MRD modules.

We also measured the time resolution for a combination of four counters piled each on another one. The average result for four counters is  $\sigma_T = 1.04$  ns. The resolution of com-

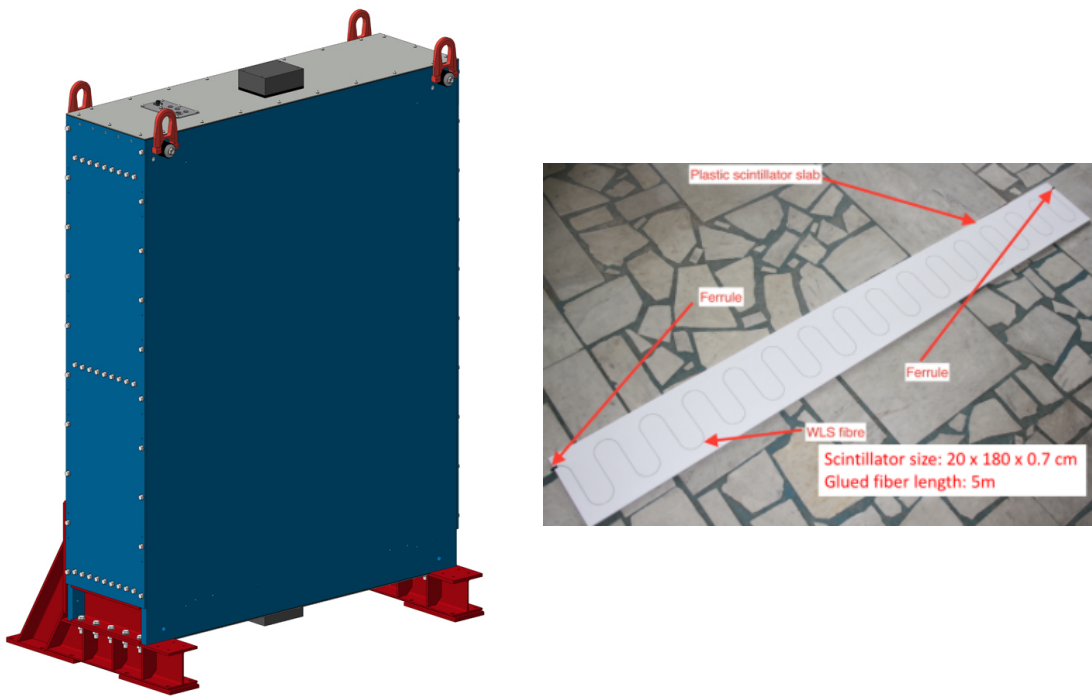


Figure 13: Left :Side-MRD module. Right: Scintillator bar of the Side-MRD modules.

290 bination of 2, 3, 4 counters is measured to be 0.79 ns, 0.66 ns and 0.58 ns, correspondently.

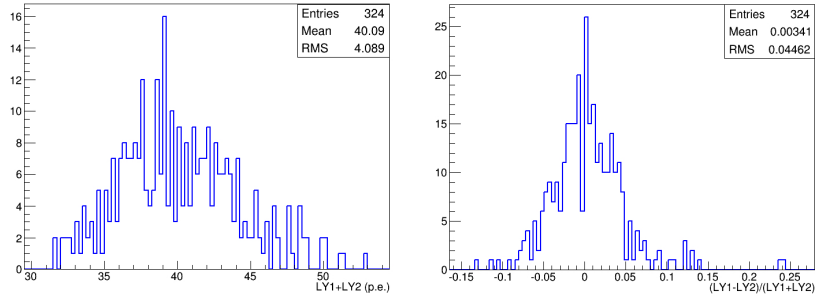


Figure 14: Total light yield distribution (left) and light yield assymetry (right) measured at YNU.

291  
292 Construction of Side-MRD modules will be done from November 2017 at Yokohama  
293 National University, then they will be transported to J-PARC and will be installed at B2  
294 floor of the T2K near detector hall.

### 295 3 Physics goals

296 We will measure the differential cross section for the charged current interaction on  $H_2O$   
297 and Hydrocarbon(CH)). The water-scintillator mass ratio of the Wagasci module is as  
298 high as 5:1 and the high purity measurement of the cross section on  $H_2O$  is possible. One  
299 experimental option is to remove water from one of the two Wagasci modules. The water-  
300 out WAGASCI module will allow to measure pure-CH target interactions with very low  
301 momentum-threshold for protons. It will also benefit to subtract the background from  
302 interaction with scintillator in the water target measurement. Another option is to add  
303 the T2K proton module which is fully made of plastic scintillators. It will allow the high  
304 statistics comparison of cross section between  $H_2O$  and CH and also comparison with  
305 the ND280 measurement. The actual configuration will be optimized with detailed MC  
306 simulation by 2018 Summer.

307 Our setup allows the measurements of inclusive and also exclusive channels such as  $1-\mu$ ,  
308  $1-\mu 1p$ ,  $1-\mu 1\pi \pm np$  samples, former two of which are mainly caused by the quasi-elastic and  
309 2p2h interaction and the latter is mainly caused by resonant or coherent pion production  
310 and deep elastic scattering. In general, an accelerator produced neutrino beam spectrum  
311 is wide and the energy reconstruction somehow rely on the neutrino interaction model.  
312 Therefore, recent neutrino cross section measurement results including those from T2K  
313 are given as a flux-integrated cross section rather than cross sections as a function of

314 the neutrino energy to avoid the model dependency. We can provide the flux-averaged  
315 cross section. In addition, by combining our measurements with those at ND280, model-  
316 independent extraction of the cross section for narrow energy region becomes possible.  
317 This method was demonstrated in [1] and also proposed by P\*\* (NUPRISM).

### 318 3.1 Expected number of events

319 Expected number of neutrino events after the event selections is evaluated with Monte  
320 Carlo simulations as we will discuss in Section 5. In the neutrino-mode,  $4.2 \times 10^3$ ,  $1.1 \times 10^3$   
321 and  $3.8 \times 10^3$  CC neutrino events are expected in the water-in WAGASCI module, the  
322 water-out WAGASCI module and the INGRID proton module after the selections with  
323  $0.5 \times 10^{21}$  POT, and its purities are 78.0 %, 97.5 % and  $\sim 98\%$ . In the antineutrino-mode,  
324  $1.7 \times 10^3$ ,  $0.4 \times 10^3$  and  $1.5 \times 10^3$  CC antineutrino events are expected in the water-in  
325 WAGASCI module, the water-out WAGASCI module and the INGRID proton module  
326 after the selections with  $0.5 \times 10^{21}$  POT, and its purities are 59.5 %, 74.4 % and  $\sim 74\%$ .

327 Statical errors of flux integrated CC-inclusive neutrino cross section measurements on  
328 H<sub>2</sub>O (full acceptance) and CH targets (forward acceptance) will be 1.5 % and 1.6 % with  
329  $0.5 \times 10^{21}$  POT in the neutrino-mode. Statical errors of flux integrated CC-inclusive an-  
330 tineutrino cross section measurements on H<sub>2</sub>O (full acceptance) and CH targets (forward  
331 acceptance) will be 2.4 % and 2.5 % with  $0.5 \times 10^{21}$  POT in the antineutrino-mode.

332 Statical errors of flux integrated H<sub>2</sub>O to CH CC-inclusive neutrino cross section ratio  
333 measurement will be 3.1 % (full acceptance) and 2.3 % (forward acceptance) with  $0.5 \times 10^{21}$   
334 POT in the neutrino-mode. Statical errors of flux integrated H<sub>2</sub>O to CH CC-inclusive  
335 antineutrino cross section ratio measurement will be 5 % (full acceptance) and 3.7 %  
336 (forward acceptance) with  $0.5 \times 10^{21}$  POT in the antineutrino-mode.

### 337 3.2 Pseudo-monochromatic beam by using different off-axis fluxes

338 The off-axis method gives narrower neutrino spectrum, and the peak energy is lower for  
339 larger off-axis angle. There still remains high energy tail mainly due to neutrinos from  
340 Kaon decay. The off-axis angle of the Wagasci location is 1.5 degree and different from the  
341 ND280 2.5 degree. Top two plots of Fig. 15 show the energy spectra of fluxes and neutrino  
342 interaction events at these two different location. The high energy tail of ND280 flux can  
343 be somehow subtraction by using the Wagasci measurement. The low energy part of the  
344 Wagasci flux can be also subtracted by using the ND280 measurement. Bottom two plots  
345 of Fig. 15 demonstrate this method. We can effectively get two fluxes, from 0.2 GeV to  
346 0.9 GeV and 0.6 GeV and 2 GeV and measure flux-integrated cross section for these two  
347 fluxes.

348 Statical errors of flux integrated CC-inclusive neutrino cross section measurements  
349 on H<sub>2</sub>O (forward acceptance) and CH targets (forward acceptance) with the pseudo-  
350 monochromatic beam will be 2 % and 1.9 % with  $0.5 \times 10^{21}$  POT in the neutrino-mode.

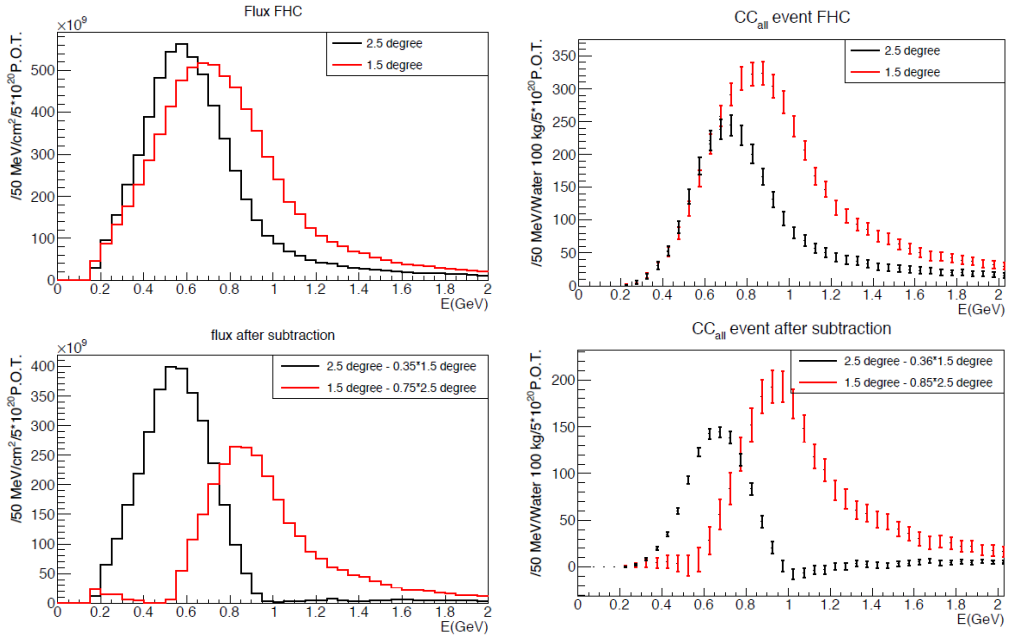


Figure 15: Energy spectra obtained by using different off-axis angle fluxes. Top two plots show the fluxes(left) and spectra of interaction events (right) for ND280 (off-axis 2.5 degree) and Wagasci (off-axis 1.5 degree). Bottom two plots show the fluxes (left) and spectra of interaction events (right) obtained by subtraction of fluxes at ND280 and Wagasci. The error bar is for the statistical error and those in the bottom right plot is obtained assuming the statistical error for ND280 measurement is much smaller than that of Wagasci experiment.

351 Statical errors of flux integrated CC-inclusive antineutrino cross section measurements  
 352 on H<sub>2</sub>O (forward acceptance) and CH targets (forward acceptance) with the pseudo-  
 353 monochromatic beam will be 3 % and 2.8 % with  $0.5 \times 10^{21}$  POT in the neutrino-mode.

### 354 3.3 Subjects Wagasci can contribute

355 In T2K experiment, neutrinos interact with bound nucleons in relatively heavy nuclei  
 356 (Carbon and Oxygen), so the cross-section is largely affected by nuclear effects. The nuclear  
 357 effects are categorized as nucleons' momentum distribution in nucleus, interactions with  
 358 correlated pairs of nucleons in nucleus (two particles-two holes, 2p2h), collective nuclear  
 359 effects calculated with Random Phase Approximation (RPA) and final state interactions  
 360 (FSI) of secondary particles in the nuclei after the initial neutrino interactions.

361 The 2p2h interactions mainly happen through  $\Delta$  resonance interactions following a

362 pion-less decay and interactions with a correlated nucleon pair. The 2p2h interactions are  
 363 observed in electron scattering experiments [5] where the 2p2h events observed in the gap  
 364 between Quasi-Elastic region and Pion-production region as shown in Fig. 16. Neutrino  
 365 experiments also attempt to measure the 2p2h interactions, but separation of the QE peak  
 366 and the 2p2h peak is more difficult because transferred momentum ( $p$ ) and energy ( $w$ )  
 367 are largely affected by neutrino energies which cannot be determined event-by-event in the  
 368 wide energy spectrum of the accelerator neutrino beam. Our model-independent narrow  
 369 neutrino spectra extracted from combined analyses of our data and ND280 data are ideal  
 370 for searching the 2p2h interaction because clearer separation of the QE peak and the 2p2h  
 371 peak is expected. Another way to observe the 2p2h interaction is direct measurement of  
 372 proton tracks in CC0 $\pi$  sample with low detection threshold and full acceptance. Fig. 17  
 373 shows proton multiplicities after FSI in CCQE events and 2p2h events, and Fig. 18 shows  
 374 opening angles among two proton tracks in the same samples. The water-out Wagasci  
 375 can provide good sample for the 2p2h interaction search because its low density medium  
 376 enables the detection of low momentum protons in addition to the full acceptance.

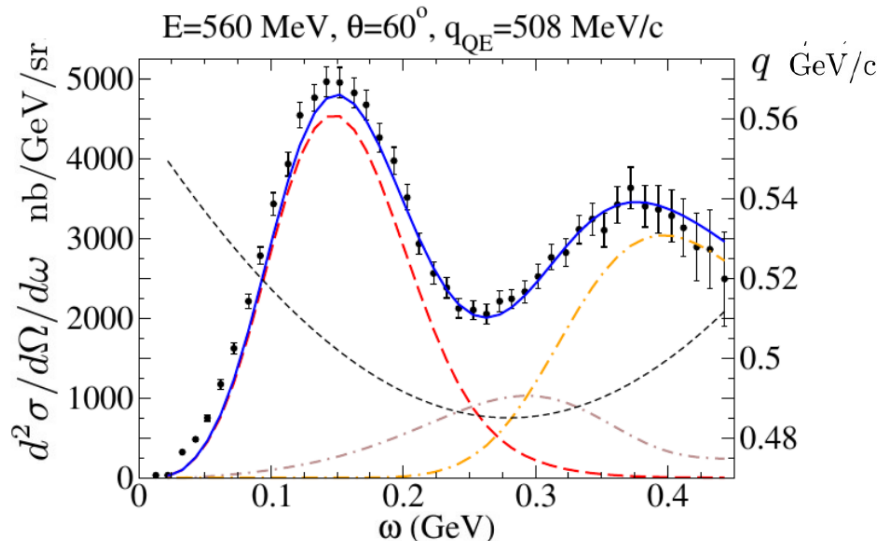


Figure 16: Comparison of inclusive  $^{12}\text{C}(\text{e},\text{e}')$  cross sections and predictions of the QE-SuSAv2 model (long-dashed red line), 2p-2h MEC model (dot-dashed brown line) and inelastic-SuSAv2 model (long dot-dashed orange line) (from Ref. [5]). The sum of the three contributions is represented with a solid blue line. The  $q$  dependence with  $w$  is also shown (short-dashed black line.)

377 The corrections from collective nuclear effects calculated by RPA as a function of  $Q^2$  are  
 378 shown in Fig. ???. The  $Q^2$  dependence of the correction can be tested by measuring angular

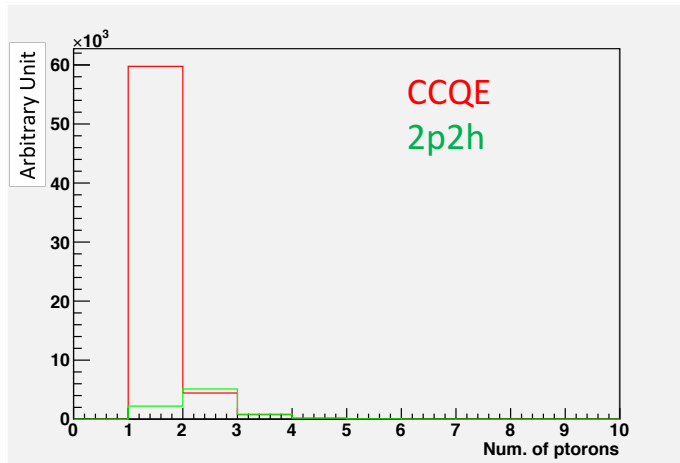


Figure 17: Proton multiplicities after FSI in CCQE events and 2p2h events.

379 distribution of muons in CC1- $\mu$  and CC1- $\mu 1p$  events. The uncertainties of the corrections  
 380 in low (high)  $Q^2$  regions can be constrained by observing the events with a forward-going  
 381 (high-angle) muon, so it is essential to measure muon tracks with full acceptance.

382 T2K experiment is starting to use  $\nu_e$  CC1 $\pi$  events for its CP violation search to increase  
 383 the statistics. One of the biggest uncertainty of the CC1 $\pi$  sample comes from the final  
 384 state interactions of pions in the nuclei after the initial neutrino interactions because they  
 385 change the multiplicity, charge and kinematics of the pions. The multi-pion production  
 386 events can be migrated into the CC1 $\pi$  sample due to the FSIs, and they become important  
 387 backgrounds. We can constrain the uncertainties from the pion FSIs by measuring pion  
 388 rescattering in the detector and pion multiplicity in  $\nu_\mu$  CCn $\pi$  sample with low detection  
 389 threshold and full acceptance for pion tracks. The water-out WAGASCI can provide good  
 390 sample for the pion FSI studies because its low density medium enables the detection of  
 391 low momentum pions in addition to the full acceptance.

## 392 4 Status of J-PARC T59 experiment

393 We had submitted a proposal of a test experiment to J-PARC in April 2014 to test a new  
 394 detector with a water target, WAGASCI, at the neutrino monitor hall, and the proposal  
 395 was approved as J-PARC T59. The project contains the side and downstream muon range  
 396 detectors as well.

397 The first WAGASCI module has been constructed in 2016 and installed at the on-  
 398 axis position in front of the T2K INGRID detector for the commissioning and the first

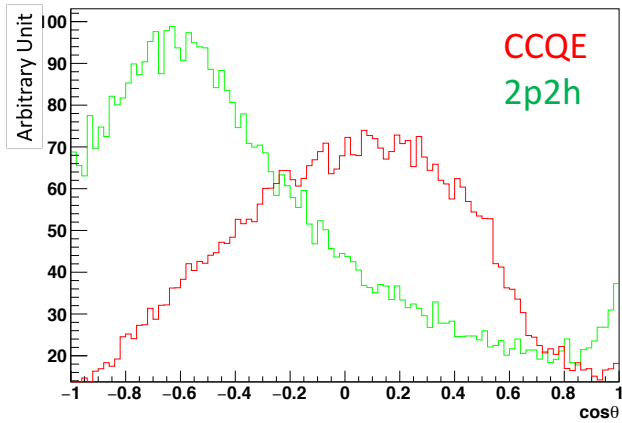


Figure 18: Opening angles among two proton tracks after FSI in CCQE events and 2p2h events.

399 cross section measurement as a part of the T2K experiment. The INGRID electronics  
 400 boards are used to read the signal. The light yield measured with muons produced by  
 401 the interaction of neutrinos in the hall wall, shown in Fig. 19, is sufficiently high to get  
 402 good hit efficiency. A track search algorithm based on the cellular automaton has been  
 403 developed using the software tools by the T2K INGRID. Examples of observed events are  
 404 shown in Fig. 20. The tracking efficiency in 2-dimensional projected plane was evaluated  
 405 by comparing the reconstructed track in the WAGASCI module and the INGRID module  
 406 and shown in Fig. 21. Note that that the tracking efficiency for high angle ( $> 70$  deg) is not  
 407 evaluated because of the acceptance of the INGRID module, not because of the limitation  
 408 of the WAGASCI module.

409 In 2017 Autumn, the construction of the second WAGASCI module and the dedicated  
 410 electronics board were completed. The module and the electronics were install to the B2  
 411 floor together with the T2K proton module and the INGRID module as shown in Fig. 22.  
 412 The proton module is to be used as the entering muon veto and also for the comparison  
 413 of interaction between CH and Water. The INGRID module is for the temporary muon  
 414 detector with limited acceptance for this period. The detector was commissioned and is  
 415 in operation to take data with the antineutrino beam during the T2K beam time from  
 416 October.

417 The production of the components of the side muon range detectors has been completed  
 418 and now the detectors are being assembled at the Yokohama National University. These  
 419 detectors will be installed sometime from January to June, 2018 when T2K is not running.

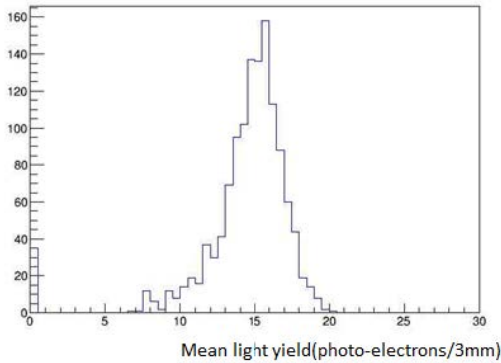


Figure 19: Light yield for muons produced by the interaction of neutrinos in the hall wall. Average light yields for each channel are plotted.

420 The Baby MIND detector was transported from CERN to Japan in December, 2017.  
 421 It will be installed and commissioned in Jan.-Feb. 2018 and T59 will take the neutrino-  
 422 induced muon data in April and May.

## 423 5 MC studies

### 424 5.1 Detector simulation

425 Expected number of neutrino events in the water-in Wagasci detector is evaluated with  
 426 Monte Carlo simulations. Neutrino beam flux at the detector location is simulated by  
 427 T2K neutrino flux generator, JNUBEAM, neutrino interactions with target materials are  
 428 simulated by a neutrino interaction simulator, NEUT, detector responses are simulated  
 429 using GEANT4-based simulation. The neutrino flux at the detector location, 1.5 degrees  
 430 away from the J-PARC neutrino beam axis, is shown in Figure 4, and its mean neutrino  
 431 energy is around 0.68 GeV.

#### 432 5.1.1 Detector geometry

433 The detector geometry in the GEANT4-based simulation is slightly different from the actual  
 434 detector as shown in Fig. 23. The active neutrino target region consists of four Wagasci  
 435 modules, and each Wagasci detector has the dimension with 100 cm  $\times$  100 cm in the x and  
 436 y directions and 50 cm along the beam direction. Two Side-MRD modules are installed at  
 437 both sides of the Wagasci modules, and each Side-MRD module consists of ten iron plates  
 438 whose dimension is 3 cm (thickness)  $\times$  200 cm (height)  $\times$  320 cm (width). The distance  
 439 between the Side-MRD modules and Wagasci modules is 80 cm. The downstream-MRD

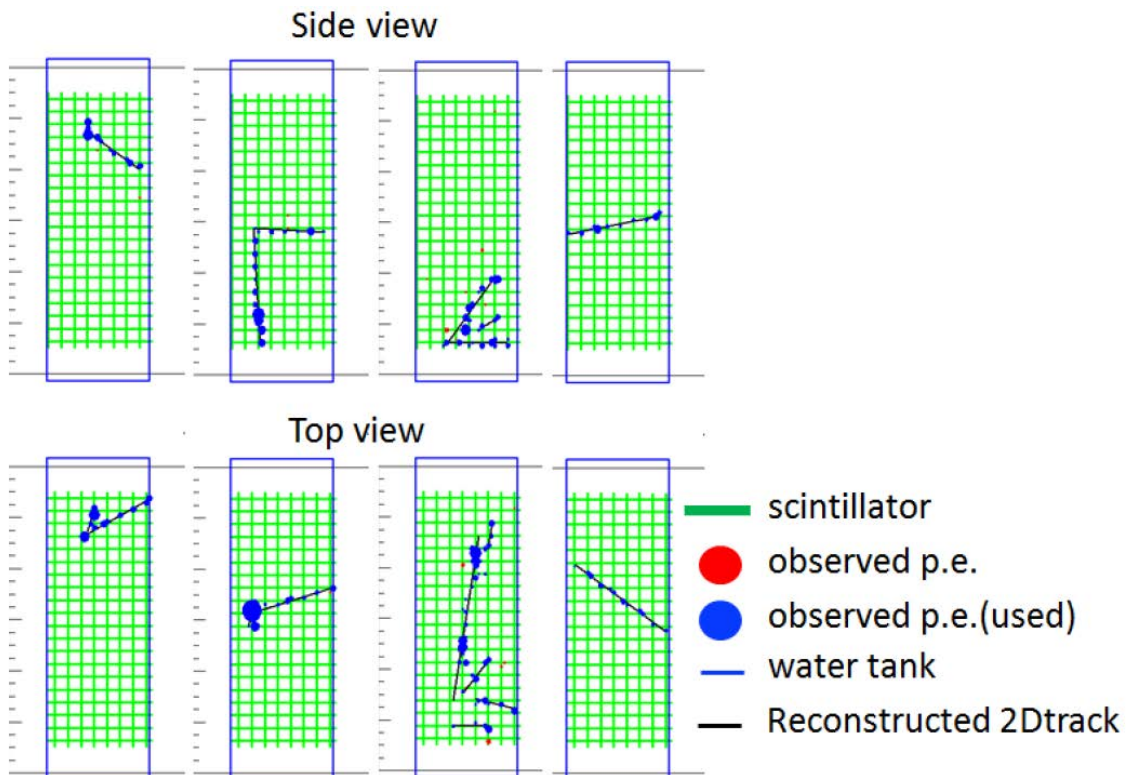


Figure 20: Example event displays of the WAGASCI module at on-axis. The reconstructed tracks are overlaid.

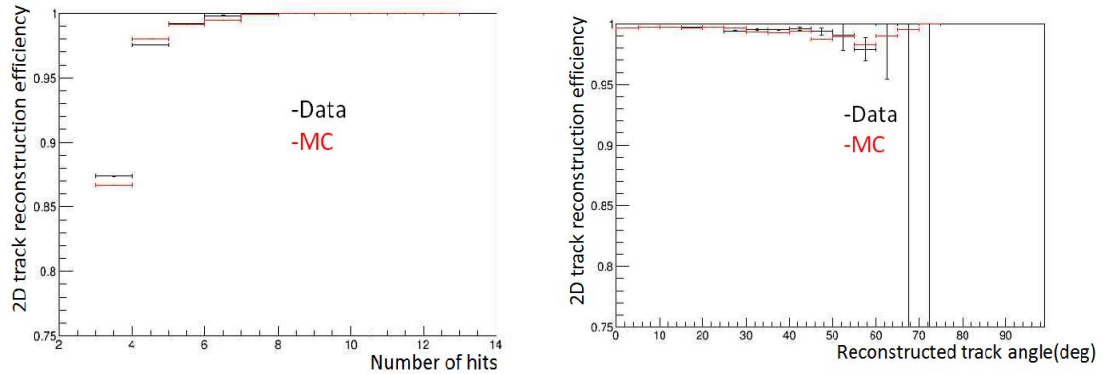


Figure 21: 2D track reconstruction efficiency as a function of number of hits (left) and track angle (right). Here the track angle is the one reconstructed by the INGRID module.

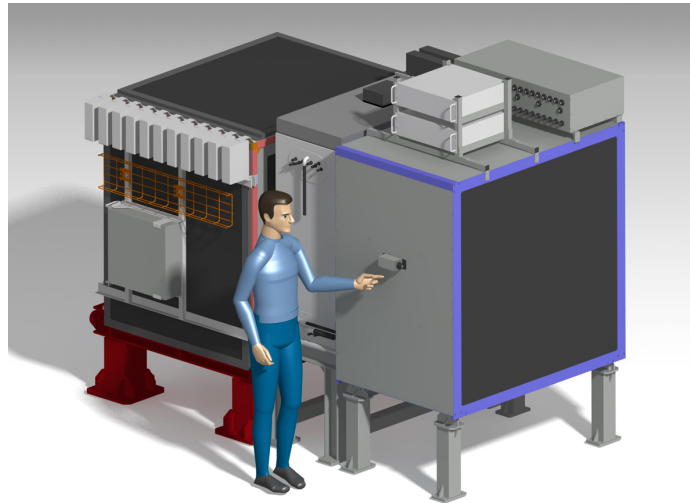


Figure 22: J-PARC T59 detector configuration in October 2017.

440 equivalent to the Baby-MIND is installed at the downstream of the Wagasci modules. The  
 441 downstream-MRD consists of thirty iron plates whose dimension is 3 cm (thickness)  $\times$  200  
 442 cm (height)  $\times$  400 cm (width). The distance between the downstream-MRD modules and  
 443 Wagasci modules is 80 cm.

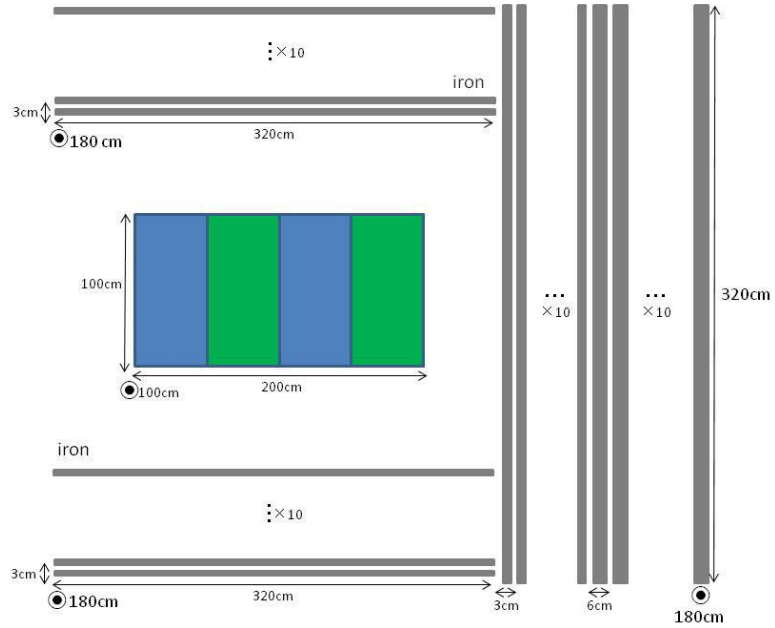


Figure 23: Geometry of the detectors in the Monte Carlo simulation.

#### 444 5.1.2 Response of detector components

445 The energy deposit inside the scintillator is converted into the number of photons. The  
 446 effects of collection and attenuation of the light in the scintillator and the WLS fiber are  
 447 simulated, and the MPPC response is also taken into account. The light yield is smeared  
 448 according to statistical fluctuations and electrical noise.

#### 449 5.2 Track reconstruction

450 To select neutrino interaction from the hit patterns, a track reconstruction algorithm is  
 451 developed. The flow of the track reconstruction is as follows.

452 1. Two-dimensional track reconstruction in each sub-detectors

- 453      2. Track matching among the sub-detectors
- 454      3. Three -dimensional track reconstruction
- 455      Add explanation about two-dim reco, track matching and three-dim reco here.

456    **5.3 Event selection**

457    First, the events with the track which starts in 5 cm from the wall of the Wagasci module  
 458    are rejected to remove the background from the outside.

459    Second, to reject backgrounds from NC and neutral particles, the longest tracks are  
 460    required to penetrate more than one (five) iron plates in Side-MRD modules (Baby-MIND).  
 461    Then, in order to measure muon momentum, the longest tracks are required to stop in  
 462    MRDs (Side-MRD modules and Baby-MIND) or penetrate all iron plates.

463    Table 1 and 2 show numbers of the selected events in one water-in Wagasci module  
 464    after each event selection in neutrino-mode and antineutrino-mode respectively. As for  
 465    the neutrino-mode, 8478 CC events are expected with  $1 \times 10^{21}$  POT, and the purity is  
 466    78.0 %. The main background for the neutrino-mode is the neutrino interactions in the  
 467    scintillators inside the Wagasci detector. As for the antineutrino-mode, 3331 CC events  
 468    are expected with  $1 \times 10^{21}$  POT, and the purity is 59.5 %. The main background for the  
 469    antineutrino-mode is the wrong sign contamination from  $\nu_\mu$  events and the antineutrino  
 470    interactions in the scintillators inside the Wagasci detector.

Table 1: Expected number of the neutrino-candidate events in one water-in Wagasci module  
 with  $1 \times 10^{21}$  POT in neutrino-mode.

Cut	CC	NC	Scinti Bkg.	Total
Reconstructed	18093.2	699.7	4698.3	23491.2
FV	15150.8	588.4	3934.8	19673.9
Pene. iron	11264.3	237.3	2875.4	14377.0
Stop/Penetrate MRDs	8478.2	214.0	2173.1	10865.2
after all cuts	78.0 %	2.0 %	20.0 %	100 %

471    Table 3 and 4 show numbers of the charged-current events in the water-in Wagasci  
 472    module after all event selection with a classification based on interactions at a vertex with  
 473     $1 \times 10^{21}$  POT in neutrino-mode and antineutrino-mode respectively.

474    Table 5 and 6 show numbers of the charged-current events in one water-in Wagasci  
 475    module after all event selection with a classification based on particles after final state  
 476    interactions with  $1 \times 10^{21}$  POT in neutrino-mode and antineutrino-mode respectively.

477    Figure 24 and 25 show the reconstructed angles of the longest tracks in the selected  
 478    events in the neutrino-mode and the anti-neutrino mode respectively. Figure 26, 27 28

Table 2: Expected number of the antineutrino-candidate events in one water-in Wagasci module with  $1 \times 10^{21}$  POT in antineutrino-mode.

Cut	CC	NC	Scinti Bkg.	Wrong sign bkg	Total
Reconstructed	6499.7	107.3	2234.4	2330.8	11172.1
FV	5457.9	89.3	1873.5	1946.6	9367.1
Pene. iron	4172.3	30.8	1440.9	1560.6	7204.6
Stop/Penetrate MRDs	3331.5	28.5	1120.3	1121.2	5601.5
after all cuts	59.5 %	0.5 %	20.0 %	20.0 %	100 %

Table 3: Expected number of the charged-current events in the water-in Wagasci module after the event selections with  $1 \times 10^{21}$  POT in neutrino-mode with a classification based on interactions at a vertex.

CCQE	MEC	CCRes	CDDIS	Total
3716.3	747.0	2081.3	1132.3	7676.9
48.4 %	9.7 %	27.1 %	14.7 %	100 %

479 and 29 show the iron plane numbers in Side-MRD and Baby-MIND corresponding to the  
 480 end points of the longest tracks in the selected events in the neutrino-mode and the anti-  
 481 neutrino mode.

#### 482 5.4 Cross section measurements on water

483 In the water target events, the background from interaction with scintillators has to be  
 484 subtracted by using the measurement of the hydrocarbon target.

Table 4: Expected number of the charged-current events in the water-in Wagasci module after the event selections with  $1 \times 10^{21}$  POT in antineutrino-mode with a classification based on interactions at a vertex.

CCQE	MEC	CCRes	CDDIS	Total
2522.0	362.8	765.8	765.8	4416.4
hline 57.1 %	8.2 %	17.3 %	17.3 %	100 %

Table 5: Expected number of the charged-current events in one water-in Wagasci module after the event selections with  $1 \times 10^{21}$  POT in neutrino-mode with a classification based on particles after final state interactions.

CC0 $\pi$	CC1 $\pi$	CC2 $\pi$	CCn $\pi$	Total
5423.1	1684.3	242.9	701.1	8051.4
67.4 %	20.9 %	3.0 %	8.7 %	100 %

Table 6: Expected number of the charged-current events in one water-in Wagasci module after the event selections with  $1 \times 10^{21}$  POT in antineutrino-mode with a classification based on particles after final state interactions.

CC0 $\pi$	CC1 $\pi$	CC2 $\pi$	CCn $\pi$	Total
2529.3	520.0	37.9	96.0	3183.2
79.5 %	16.3 %	1.2 %	3.0 %	100 %

485    **5.4.1 Charged current cross section measurement**

486    **6 Standalone WAGASCI-module performances**

487    In the previous sections, the WAGASCI detector was studied using the Muon Range Detectors. In this section, the standalone abilities of WAGASCI module are presented. Using  
 488    the WAGASCI configuration presented in Section 5, we have evaluated that only 7% of  
 489    the muons will be stopped in one of the WAGASCI modules. THowerver, this proportion  
 490    increases to 53% for pions and 73% for protons produced by neutrino interactions at  $1.5^\circ$   
 491    off-axis. Figure 30 shows the momentum distribution of these daughter particles as well as  
 492    for the sub-sample stopped in one of the WAGASCI modules. Therefore, the study of the  
 493    standalone abilities of the WAGASCI module in this section are dominantly motivated by:  
 494   

- 495    • the accurate measurement of the neutrino interaction final states. Though most of the  
 496    muons will be reconstructed and identified in the MRDs, the hadronic particles will  
 497    predominantly stops in one WAGASCI module. One has therefore to rely exclusively  
 498    on the WAGASCI module information alone to reconstruct, identify and measure the  
 499    momentum of pions or protons.
- 500    • the coverage of the MRDs is not  $4\pi$ . Using the WAGASCI module information can  
 501    therefore help to constraint the particles that exits the WAGASCI module but do  
 502    not geometrically enters any MRD.
- 503    • the particle identification of low momenta muons  $p_\mu < 300$  MeV/c that will leave only  
 504    few hits in the MRD. Using the WAGASCI module information will clearly enhance

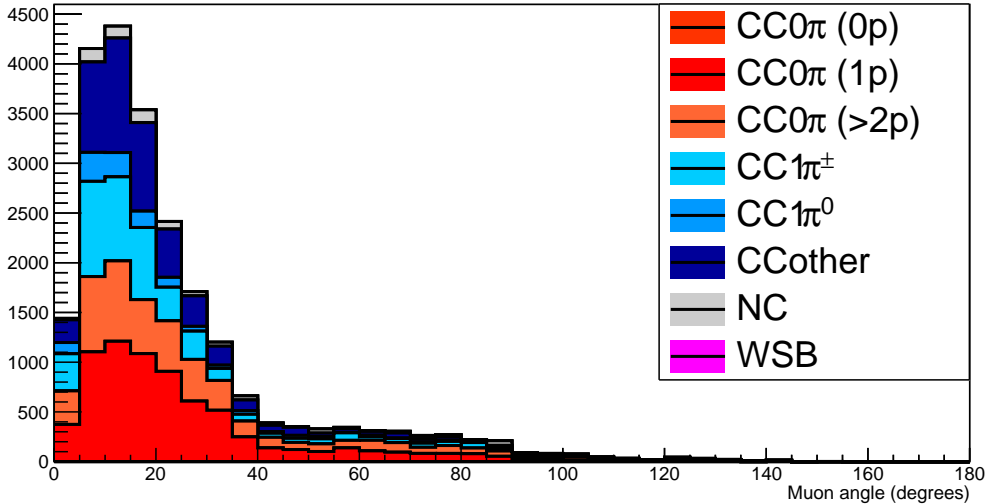


Figure 24: The reconstructed angles of the longest tracks in the selected events in the neutrino-mode.

505 the particle identification.

506 This study is based on an original study done for the ND280 upgrade target, with some  
 507 modifications. Though the cell size is similar to the WAGASCI configuration presented  
 508 in Section 5, the external dimensions are different ( $186.4 \times 60 \times 130 \text{ cm}^3$ ). Whenever the  
 509 results are presented with this external size and this parameter is likely to impact the  
 510 result, it will be mentioned.

511 Note that in this section, a simplified reconstruction algorithm presented in Section 6.1 is  
 512 used. The fiducial volume is chosen accordingly as the inner cube of the module which  
 513 surfaces are distant of  $4 \times$  scintillator space = 10 cm from the module external surfaces.

514 The neutrino interactions are simulated using NEUT v5.3.2. The NEUT input neutrino  
 515 flux is estimated using JnuBeam v13a and assuming the detector to be located at  $1.5^\circ$   
 516 off-axis, as in Section 5. Note that the event reconstruction efficiency as a function of true  
 517 neutrino energy might be changed at  $1.5^\circ$ , due for example to different  $Q^2$  distributions. For  
 518 this reason, one has to note that the reconstruction results might slightly be changed from  
 519  $2.5^\circ$  and  $1.5^\circ$ . To avoid a similar change on the particle-only reconstruction efficiencies,  
 520 they will be presented as a function of variables that completely characterize the particle  
 521 kinematic state, *i.e.* its momentum and angle. Figure 31 shows the vertices distributions  
 522 of the daughter particles of neutrinos interacting one standard WAGASCI water-module.

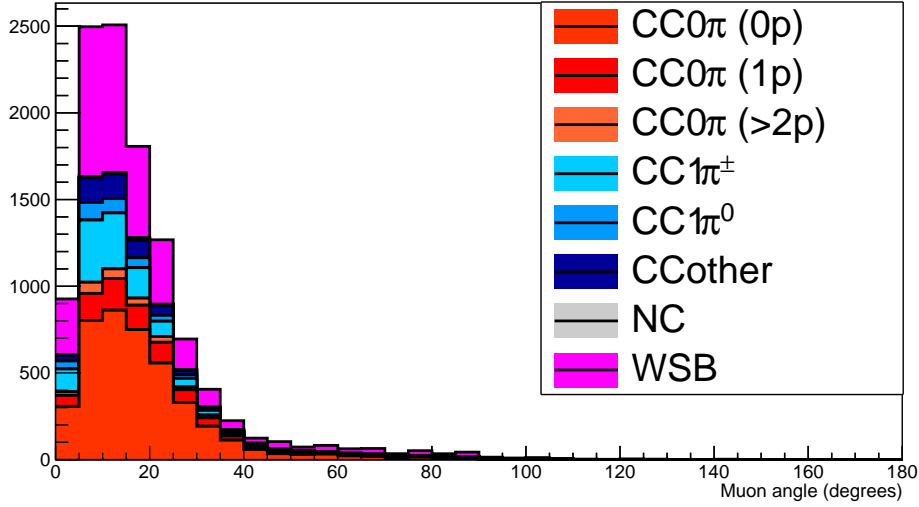


Figure 25: The reconstructed angles of the longest tracks in the selected events in the antineutrino-mode.

523 In this section, we will show the detector reconstruction and particle identification in this  
 524 phase space, both for leptonic and hadronic particles. We will finally show an empty  
 525 WAGASCI module can highly enhance the ability to constrain the neutrino interaction  
 526 final state which is critical to reduce the corresponding uncertainties.

527 **6.1 Reconstruction algorithm**

528 **6.1.1 Description**

529 For this section, an ideal “simulated” reconstruction is developed. A particle is recon-  
 530 structed if:

531 1. The particle is charged.

532 2. Lets at least one hit (energy deposit  $> 2.5$  photo-electron) in a scintillator.

533

534 3. The particle enters one TPC and let one hit in the tracker.

535 Or

536

- 537 • The particle should be long enough to be reconstructed by the detector in at  
 538 least 2 out of 3 views (XZ, YZ, XY). The length criterion requires the particle

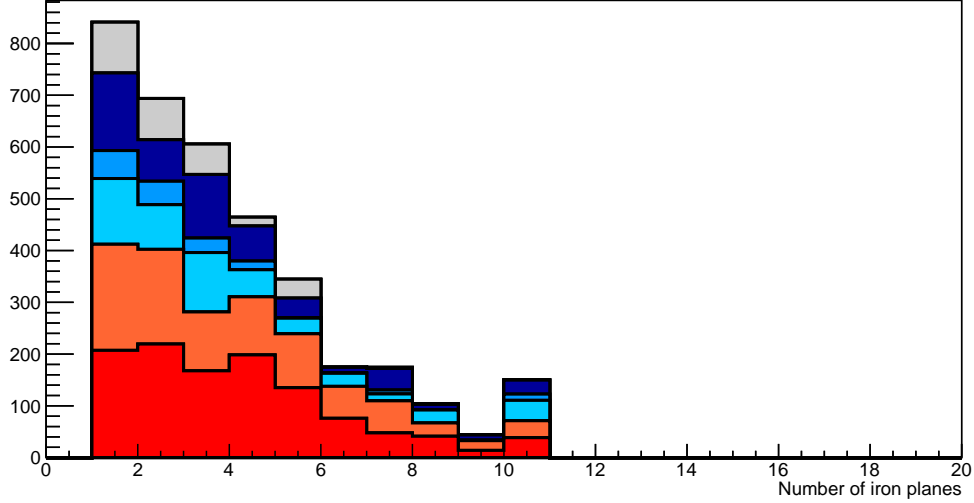


Figure 26: Iron plane numbers in Side-MRD corresponding to the end points of the longest tracks in the selected events in the neutrino-mode.

539  
540  
541

to let at least 4 hits in the detector. In the “less favourable case” of pure longitudinal or transverse going tracks, it represents a the track length of  $L_{track} \geq 4 \times$  scintillator space = 10.0 cm.

542  
543  
544  
545  
546  
547  
548  
549  
550  
551

- In the views where particles pass the length criterion, the particle shall not be superimposed with longer tracks in at least two views. The superposition criterion is estimated with the distance inter-tracks (DIT) which corresponds to the orthogonal distance between two tracks at the ending point of the shortest one (see Figure 32). For a track 1, the superposition criterion is tested with every longer tracks that starts at the same vertex. Let  $\vec{p}_1$  the vector of track 1, and  $p_1^a$  its projections in the XZ, YZ and XY planes respectively for  $i=1,2,3$ . Note that these are projections in a 2D planes and not on a direction vector. In this case, the relative angle between the track 1 and a longer track 2 (of vector  $\vec{p}_2$ ) in a view a is given by:

$$\cos \theta = \frac{\vec{p}_1^a \cdot \vec{p}_2^a}{\|\vec{p}_1^a\| \|\vec{p}_2^a\|} \quad (1)$$

552

and the distance inter track is given by:

$$DIT = \|\vec{p}_1^a\| \sin \theta \quad (2)$$

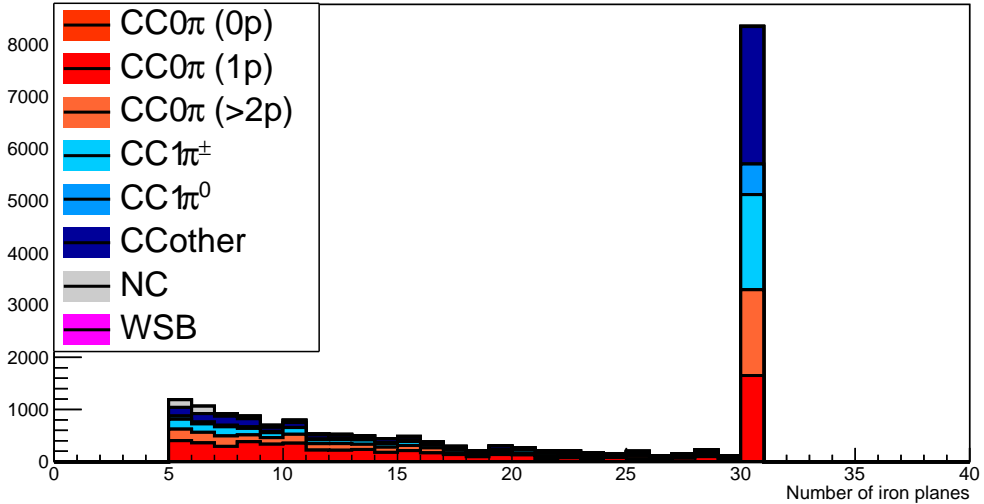


Figure 27: Iron plane numbers in Baby-MIND corresponding to the end points of the longest tracks in the selected events in the neutrino-mode.

553            The DIT should be higher than  $4 \times$  scintillator width for the track 1 to be not  
 554            superimposed with the track 2 in the view a, which also corresponds to 10.0 cm  
 555            in the nominal configuration.

### 556        6.1.2 Performances

557        The particle-only reconstruction efficiencies and the reconstruction threshold in momenta  
 558        are shown in Table 7. This threshold is defined as the maximal momentum for which the  
 559        reconstruction efficiency is smaller than 30%. The thresholds in muon and pion momenta  
 560        are 150 MeV/c. Most of the muons are above this threshold (see Figure 31) which leads  
 561        to a 79% reconstruction efficiency.

562        The lower pion and proton efficiencies (respectively 52% and 26%) are due to lower  
 563        efficiencies for similar momenta than muons, coming from strong interactions as shown  
 564        on Figures 33. Efficiencies of each particle type tend to decrease in the backward region  
 565        due to particle lower momenta. However, for a fixed momentum value, the reconstruc-  
 566        tion efficiency is almost uniform which confirms the ability of the WAGASCI detector to  
 567        reconstruct high angle tracks.

568        The reconstruction is thereafter tested on neutrino events. Table 8 summarizes the  
 569        number of reconstructed events and efficiencies for each interaction type. As expected

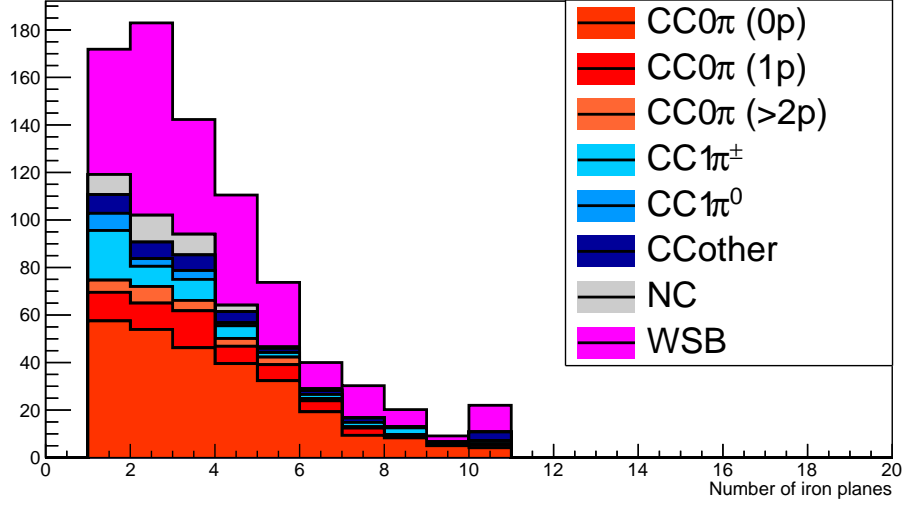


Figure 28: Iron plane numbers in Side-MRD corresponding to the end points of the longest tracks in the selected events in the antineutrino-mode.

	$\mu$	$\pi$	p
Reconstruction Efficiency Momentum threshold	79% 150 MeV/c	52% 150 MeV/c	26% 550 MeV/c

Table 7: Reconstruction efficiency and momentum threshold for muons, pions and protons. The threshold is defined as the maximal momentum for which particles have a reconstruction efficiency smaller than 30%.

570 from the high muon reconstruction efficiency, the charged current interactions have recon-  
571 struction efficiencies  $\geq 85\%$ .

572 The reconstruction efficiencies as a function of the neutrino energy and muon kinematics  
573 are respectively shown on Figure 34 and 35.

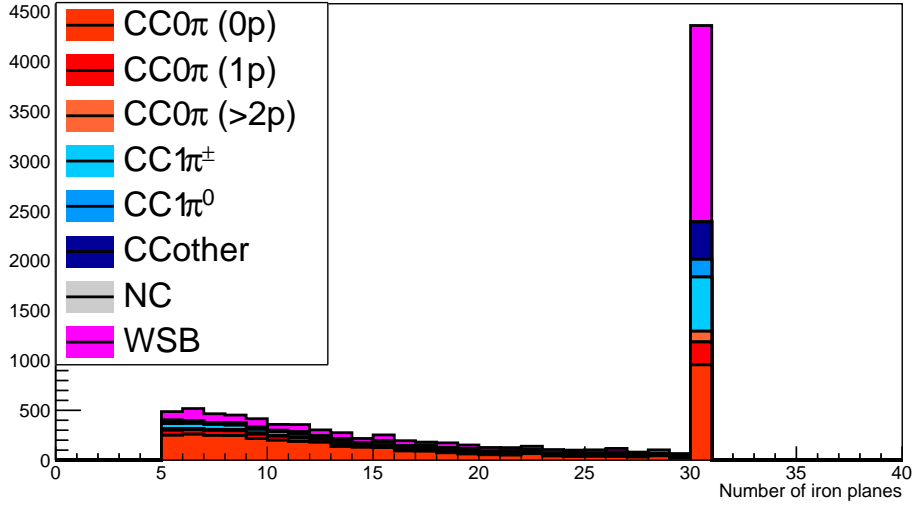


Figure 29: Iron plane numbers in Baby-MIND corresponding to the end points of the longest tracks in the selected events in the antineutrino-mode.

	CC0π	CC1π	CCOthers	NC	All
Reconstruction efficiency	85%	87%	91%	22%	68%

Table 8: Number of true interactions reconstructed. The purity and reconstruction efficiency of each true interaction is also shown.

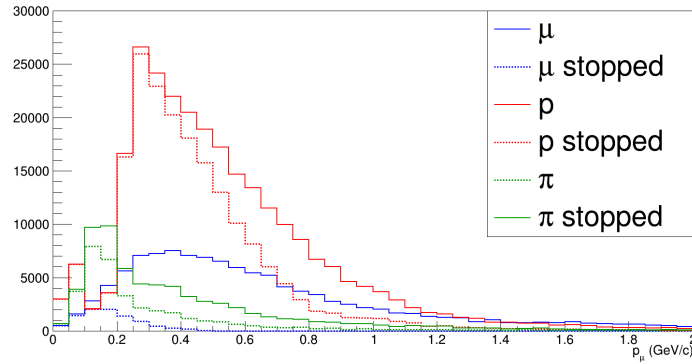


Figure 30: Momentum distribution of true particles in WAGASCI (plain) and corresponding distributions only for particles stopping into the WAGASCI module (dashed).

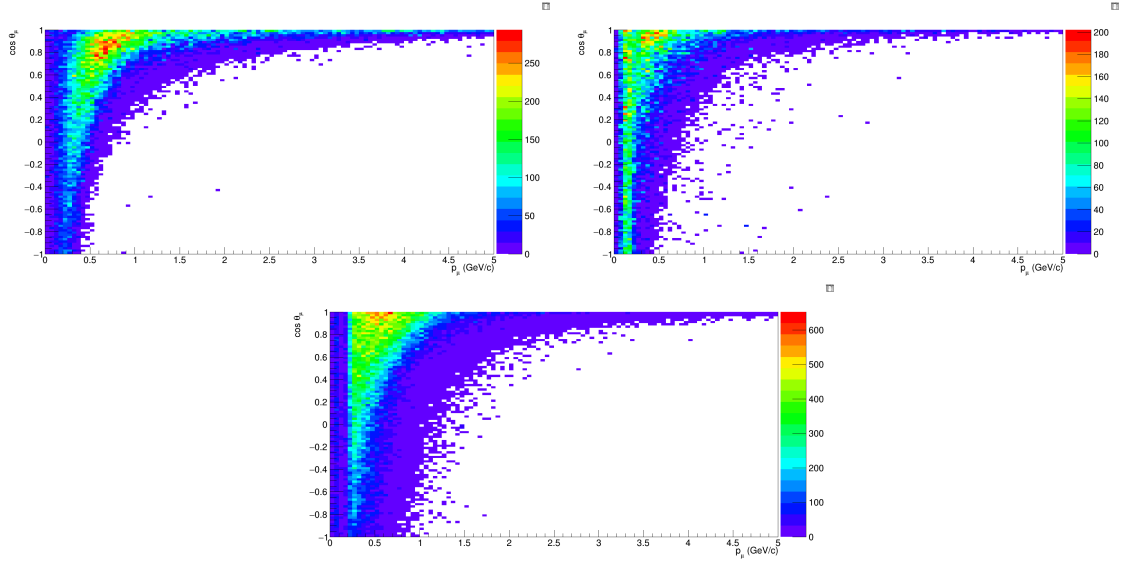


Figure 31: True number of muons (left), charged pions (right) and protons (bottom) in the two WAGASCI water-module as a function of the particles momenta and angles at  $1.5^\circ$ .

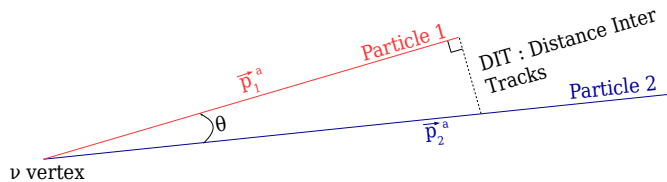


Figure 32: Definition of the distance inter tracks.

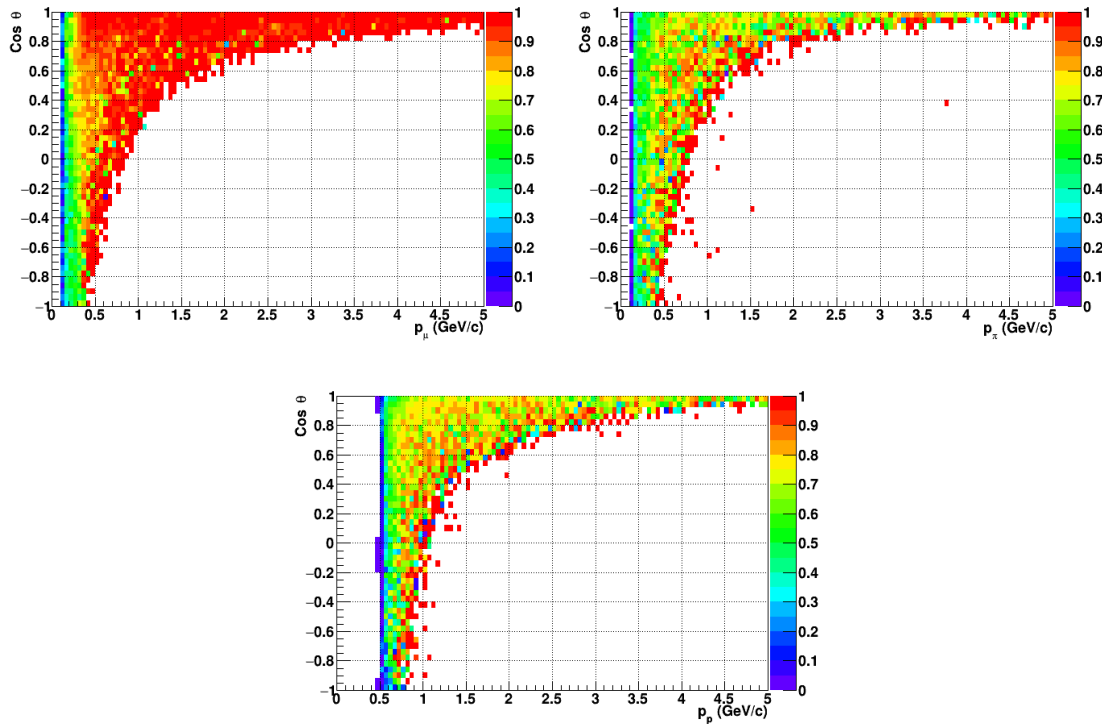


Figure 33: Reconstruction efficiency of muons (left), charged pions (right) and protons (bottom) in the WAGASCI water-module as a function of the particles momenta and angles.

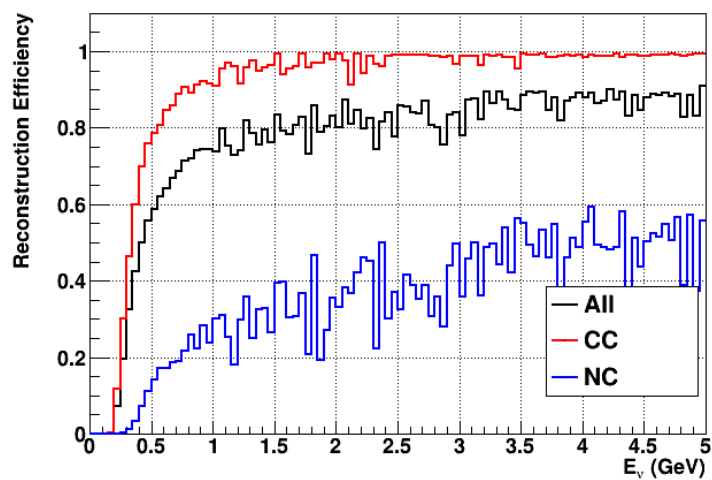


Figure 34: Reconstruction efficiency of all neutrino (black), CC (red) and NC (blue) interactions in the WAGASCI water-module as a function of the neutrino energy.

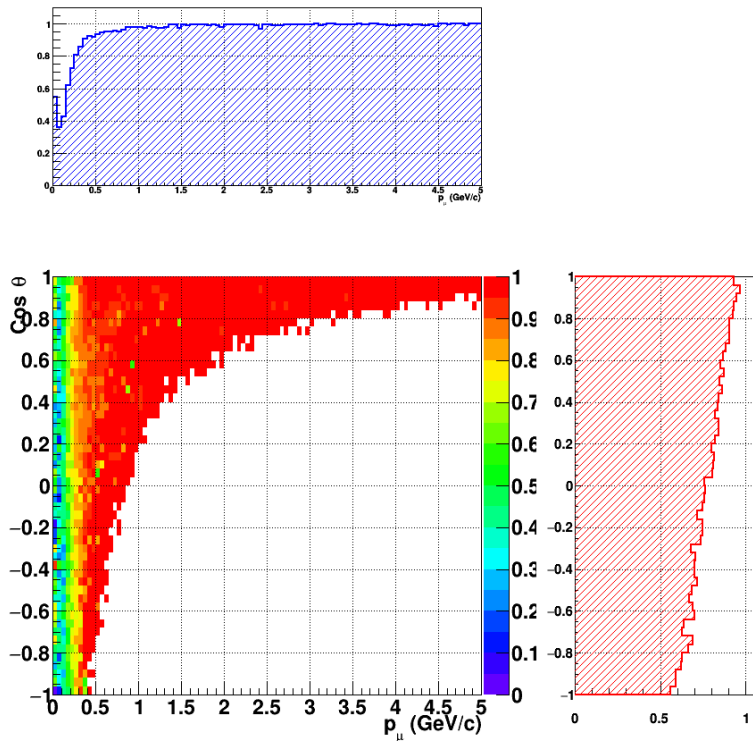


Figure 35: Reconstruction efficiency of CC interactions in the WAGASCI water-module as a function of the muon kinematic variables (momentum and angle).

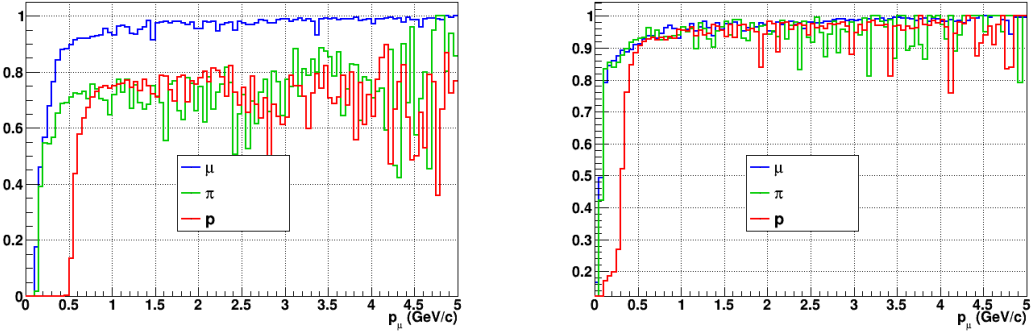


Figure 36: Reconstruction efficiency for muons, pions and protons in the water-in (left) and water-out (right) modules.

574 Note that a Particle Identification Algorithm has been also developed. It is based on  
 575 the charge deposition of the particles in the scintillator, of the detection of a decay-electron.  
 576 However, this information highly depends on the number of scintillator hit by a particle,  
 577 which creates an important difference between a real WAGASCI module and the one used  
 578 for the ND280-upgrade simulation. For this reason, the corresponding results will not be  
 579 detailed here, but can be found in [?].

## 580 6.2 Background subtraction: the water-out module

581 In the nominal configuration, 20% of the neutrino interactions occurs on scintillators  
 582 ( $C_8H_8$ ). This background should be removed in order to measure the neutrino interac-  
 583 tion on the same target as Super-K, which suppress the differences in cross-section models.  
 584 For this purpose, we propose to use a water-out module, where the water is replaced by  
 585 air. The detector is therefore fully active and has a 3 mm spatial resolution (scintillator  
 586 thickness) which create an ideal detector to reconstruct and identify hadrons, and study  
 587 np-nh interactions. The counter-part is the difference in particle energy deposition between  
 588 the water and this water-out module that will need to be corrected for. In this section,  
 589 we present the capabilities of such a module, and the impact it can have on cross-section  
 590 measurements for the neutrino community in general and T2K in particular.  
 591 The same reconstruction and selection as the water-in module is applied. Figure 36 shows  
 592 the comparison between the water-in and the water-out reconstruction efficiencies for muon,  
 593 pions and protons. 90% of the muons and 87% of the pions are reconstructed, while 70%  
 594 of the protons are even reconstructed. It allows to lower down the proton threshold to  
 595 250 MeV/c (see Table 9).

596 As a consequence of tracking even low momenta particle, the reconstruction efficiency  
 597 is uniform and almost maximal on the entire  $\cos \theta_\mu$  phase space, as shown on Figure 37.

	$\mu$	$\pi$	p
Reconstruction Efficiency Momentum threshold	90% 50 MeV/c	87% 50 MeV/c	70% 250 MeV/c

Table 9: Reconstruction efficiency, proportions of  $\mu$ -like and non  $\mu$ -like and momentum threshold for muons, pions and protons in the empty module. The threshold is defined as the maximal momentum for which particles have a reconstruction efficiency smaller than 20%.

598 Since the fiducial mass represents 0.25 tons, the total number of events is divided by a  
 599 factor of 3 compared to the water-in module. The water-out module offers interesting  
 600 possibilities to study np-nh interaction since 70% of the protons are reconstructed. In the  
 601 future, a possible separation as a function of the number of proton track will be studied.  
 602 Moreover, we are currently pursuing the use of single and double transverse variables (cite  
 603 Xianguo) to open new possibilities for separating np-nh from Final State Interactions, or  
 604 for isolating the interactions on hydrogen from interactions on carbon in this module.

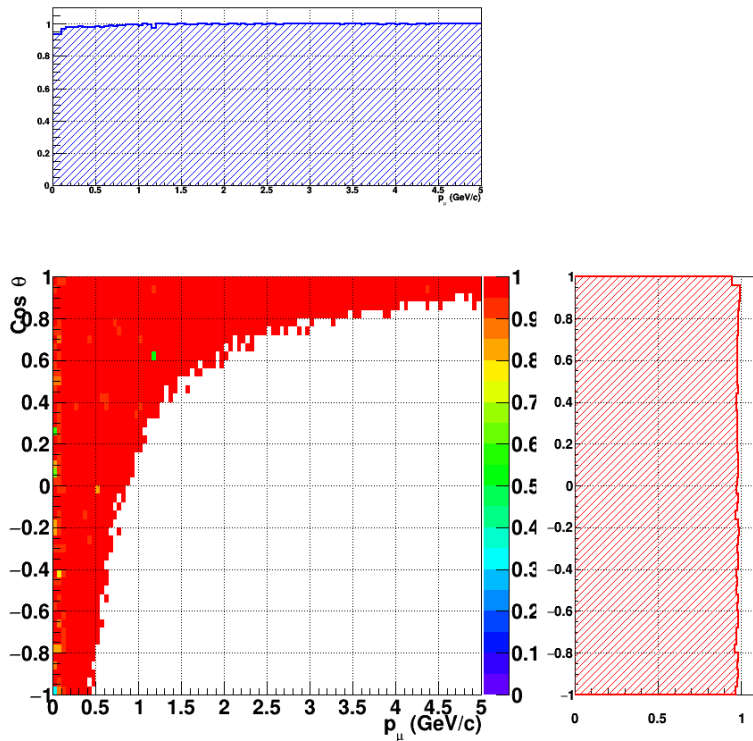


Figure 37: Reconstruction efficiency of CC interactions in the WAGASCI empty module as a function of the muon kinematic variables (momentum and angle).

605 **7 Schedule**

606 We would like to start a physics data taking from T2K beam time after the summer  
607 shutdown in 2018. By then, commissioning and tests of the detectors will be completed  
608 in J-PARC T59. The experiment can run parasitically with T2K, therefore we request no  
609 dedicated beam time nor beam condition as discussed in the following section.

610 Once the approved POT is accumulated, the WAGASCI modules will be removed  
611 from the experimental site, but we would like to keep the Baby-MIND and the Side-MRD  
612 modules on the B2 floor of the NM pit as common platforms of future neutrino experiments  
613 using the T2K neutrino beam.

614 **8 Requests**

615 **8.1 Neutrino beam**

616 The experiment can run parasitically with T2K, therefore we request no dedicated beam  
617 time nor beam condition. As data taking periods, we request the ‘nominal’ T2K one-year  
618 operation both for the neutrino beam and the antineutrino beam. The T2K has been  
619 requesting  $0.9 \times 10^{21}$  POT/year and actually accumulating about  $0.7 \times 10^{21}$  POT/year in  
620 recent years. For each year, starting from the Autumn, T2K is running predominantly in  
621 the neutrino mode or in the antineutrino mode. Our request is to have one-year neutrino-  
622 mode data and another one-year antineutrino mode data assuming that the POT for the  
623 fast extraction in each year is more than  $0.5 \times 10^{21}$  POT.

624 **8.2 Equipment request including power line**

625 We request the followings in terms of equipment on the B2 floor:

- 626 • Site for the WAGASCI modules, Side-MRD modules and BabyMIND and their elec-  
627 tronics system on the B2 floor of the near detector hall (Fig. 3).
- 628 • Anchor points (holes) on the B2 floor to secure the WAGASCI modules, Side-MRD  
629 module and Baby-MIND (Fig. ??)
- 630 • Power line for the magnets in Baby-MIND: 400 V tri-phase 48-to-62 Hz, capable of  
631 delivering 12 kW.
- 632 • Electricity for electronics and water circulation system, 3 kW, standard Japanese  
633 electrical sockets.
  - 634 1. Online PCs: 2.1 kW
  - 635 2. Electronics: 0.7 kW
  - 636 3. Water sensors: ?

- 637     • Air conditioner for cooling heat generation at Baby-MIND magnets, online PCs and  
638        electronics
- 639     • Beam timing signal and spill information
- 640     • Network connection

641 **8.2.1 Baby MIND Equipment request including power line**

642 We request the following in terms of equipment on the B2 floor:

- 643     • Site for the Baby MIND detector and its electronics systems on the B2 floor of the  
644        near detector hall.
- 645     • Anchor points (holes) on the B2 floor to secure the 9 support frames, of order 4 holes  
646        per frame, detailed floor plans to be communicated in a separate document.
- 647     • Power line for the magnet: 400 V tri-phase 48-to-62 Hz, capable of delivering 12  
648        kW. We have a wish for the magnet power line to be installed and available to us by  
649        beginning of March 2018.
- 650     • Electricity for electronics, 1 kW, standard Japanese electrical sockets.
- 651     • Beam timing signal and spill information
- 652     • Network connection

653 The infrastructure for much of the above exists already, and will be shared in part with  
654 the WAGASCI experiment. Exceptions are the power line for the magnet and holes in the  
655 B2 floor to anchor the detector support structures.

656 **9 Conclusion**

657 **References**

- 658 [1] K. Abe et al. Measurement of the muon neutrino inclusive charged-current cross sec-  
659        tion in the energy range of 13 GeV with the T2K INGRID detector. *Phys. Rev.*,  
660        D93(7):072002, 2016.
- 661 [2] M. Antonova et al. Baby MIND Experiment Construction Status. In *Prospects in*  
662        *Neutrino Physics (NuPhys2016) London, London, United Kingdom, December 12-14,*  
663        2016, 2017.
- 664 [3] K. Nitta et al. The k2k scibar detector. *Nucl. Instrum. Meth. A*, 535:147, 2004.

- 665 [4] J. Fleury, S. Callier, C. de La Taille, N. Seguin, D. Thienpont, F. Dulucq, S. Ahmad,  
666 and G. Martin. Petiroc and Citiroc: front-end ASICs for SiPM read-out and ToF  
667 applications. *JINST*, 9:C01049, 2014.
- 668 [5] M. B. Barbaro J. A. Caballero T. W. Donnelly G. D. Megias, J. E. Amaro. Inclusive  
669 electron scattering within the susav2 meson-exchange current approach. *Phys. Rev. D*,  
670 94:013012, 2016.
- 671 [6] Yu. G. Kudenko, L. S. Littenberg, V. A. Mayatsky, O. V. Mineev, and N. V. Ershov.  
672 Extruded plastic counters with WLS fiber readout. *Nucl. Instrum. Meth.*, A469:340–  
673 346, 2001.
- 674 [7] O. Mineev, Yu. Kudenko, Yu. Musienko, I. Polyansky, and N. Yershov. Scintillator  
675 detectors with long WLS fibers and multi-pixel photodiodes. *JINST*, 6:P12004, 2011.
- 676 [8] Etam Noah et al. Readout scheme for the Baby-MIND detector. *PoS*, Pho-  
677 toDet2015:031, 2016.